Article

Discovery Medicine 2025; 37(201): 2455–2474
https://doi.org/10.24976/Discov.Med.202537201.207

Sodium Hydrosulfide Alleviates Osteoporosis by Suppressing Osteoclastogenesis via the Inhibition of the NF-κB Signaling

Wenqing Tong[1,†], Wenchao Fei[1,†], Ke Xu[1], Yang Hong[1,2,3,*], Yinghua Li[4,*]

[1]Department of Orthopedics, The Fifth People's Hospital of Shanghai, Fudan University, 200040 Shanghai, China
[2]Shanghai Clinical Research Center for Aging and Medicine, 200040 Shanghai, China
[3]Center of Community-Based Health Research, Fudan University, 200040 Shanghai, China
[4]Central Laboratory, The Fifth People's Hospital of Shanghai, Fudan University, 200040 Shanghai, China
*Correspondence: hongyang@fudan.edu.cn (Yang Hong); zhulihan@fudan.edu.cn (Yinghua Li)
[†]These authors contributed equally.
Submitted: 30 May 2025 Revised: 2 September 2025 Accepted: 4 September 2025 Published: 20 October 2025

Background: While existing pharmacotherapies for osteoporosis, such as bisphosphonates, reduce fracture risk, their long-term use remains limited by adverse effects, including gastrointestinal toxicity, osteonecrosis of the jaw, and atypical femoral fractures. Hydrogen sulfide (H_2S), an endogenous gasotransmitter with anti-inflammatory properties, emerges as a potential alternative, but the role of its donor, sodium hydrosulfide (NaHS), in osteoporosis remains unexplored. Therefore, this study investigates NaHS-driven bone-protective mechanisms, emphasizing its ability to modulate the nuclear factor kappa-B (NF-κB)/ inhibitor of NF-κB alpha (IκB-α) axis—a crucial pathway in osteoclastogenesis.

Methods: Mice were divided into a sham control group (n = 6) and an ovariectomized (OVX) group (n = 6). Mice in the OVX group received varying doses of NaHS (0, 0.38, 0.75, 1.5 mg/kg/day) or vehicle for 4 weeks. Bone mineral density (BMD) was quantified using micro-computed tomography (micro-CT) analysis. Osteoclast differentiation was assessed in bone marrow-derived macrophages (BMMs) and RAW264.7 cells via tartrate-resistant acid phosphatase (TRAP) staining. Molecular mechanisms were deciphered using ubiquitination assays, nuclear/cytoplasmic fractionation, and immunofluorescence.

Results: NaHS treatment increased lumbar BMD and trabecular bone-to-tissue volume in OVX mice compared to untreated controls. *In vitro*, NaHS (0.15 mM) significantly suppressed receptor activator of nuclear factor-κB ligand (RANKL)-induced osteoclastogenesis ($p < 0.05$). Mechanistically, for the first time, NaHS was found to stabilize IκB-α by inhibiting its ubiquitination, thereby blocking the nuclear translocation of NF-κB p65.

Conclusions: NaHS mitigates OVX-induced bone loss via dual inhibition of osteoclast differentiation (through IκB-α/NF-κB blockade) and bone resorption. Its capacity to circumvent the limitations of current therapies positions NaHS as a novel candidate for osteoporosis management.

Keywords: NaHS; osteoporosis; osteoclastogenesis; NF-κB; IκB-α; potential therapeutics

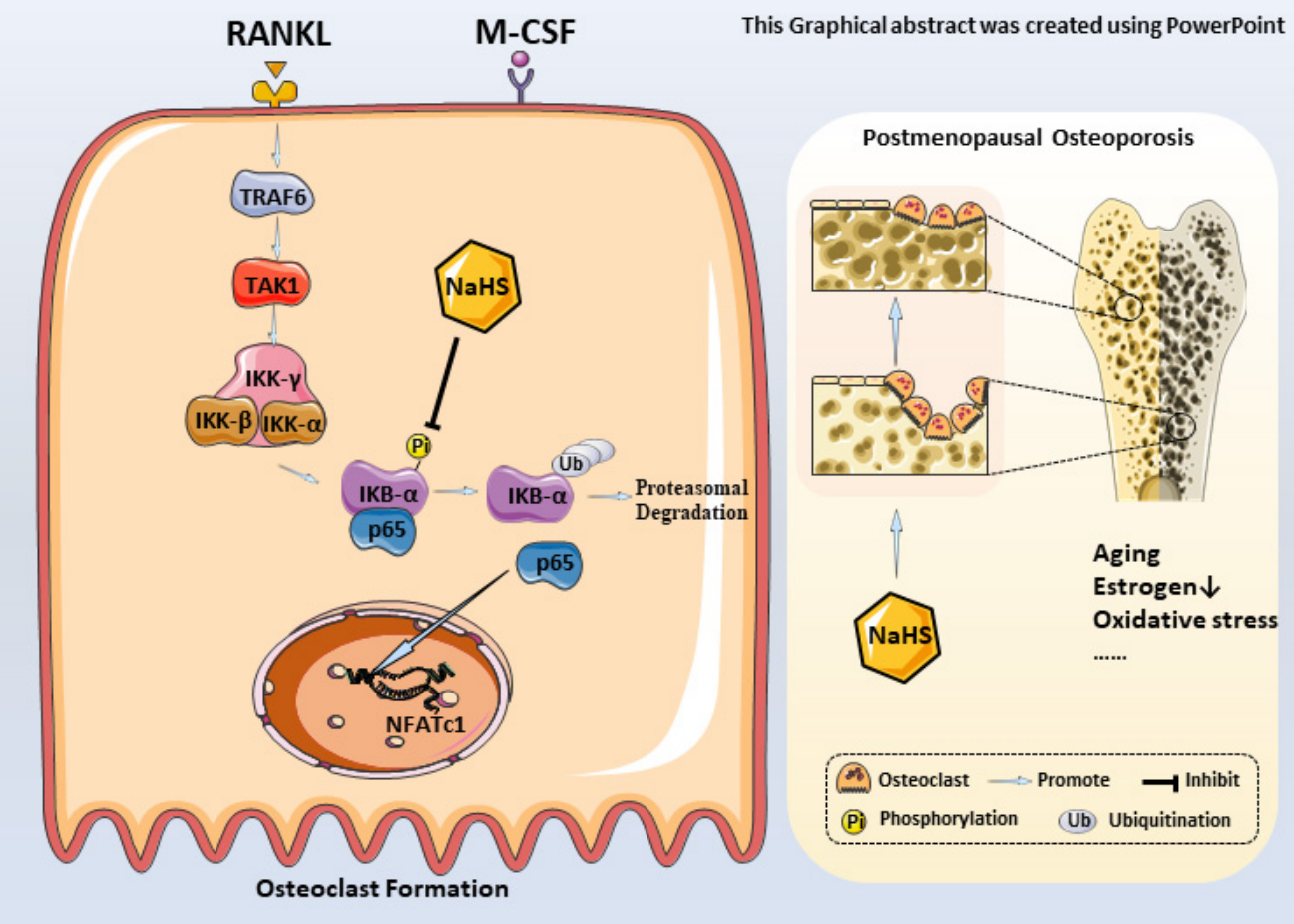

Graphical Abstract.

Introduction

Osteoporosis is a metabolic bone disease characterized by decreased bone mass and destruction of bone microstructure [1]. It is broadly categorized into primary and secondary types. Primary osteoporosis often occurs in postmenopausal women, where elevated osteoclast activity, without a corresponding increase in osteoblast function, leads to enhanced bone dissolution effect and subsequent bone fragility [2]. The diagnosis strategies and treatment modalities for osteoporosis have advanced; they are still inadequate compared to those available for diseases such as diabetes and need further optimization [3]. Currently, the most commonly used treatment for osteoporosis includes bisphosphonates, receptor activator of nuclear factor-κB ligand (RANKL) monoclonal antibodies, and hormone replacement therapy (HRT). These treatment approaches primarily target osteoclasts to inhibit their formation and bone-resorption activity. However, prolonged estrogen therapy increases the risk of malignancies in women, such as breast cancer and endometrial cancer [4]. Similarly, long-term use of bisphosphonates has many adverse outcomes, such as atypical non-healing bone fractures, osteonecrosis of the jaw, and even a decrease in bone strength [5]. These limitations highlight the challenges in current anti-osteoporosis therapeutics and emphasize the urgent need for novel drug development to improve both treatment and prognostic outcomes.

Throughout the human life cycle, bones undergo continuous remodeling to maintain dynamic balance, a process that depends on the synergistic activity of osteoclast and osteoblast [6]. Osteoclasts are responsible for bone resorption, but they also play a vital role in new bone formation [7]. During early menopause, osteoclastogenesis is dysregulated, resulting in bone trabecular perforation and loss of structural connectivity [8].

Osteoclasts originate from myeloid hematopoietic precursors, and RANKL primarily promotes their differentiation; RANKL promotes differentiation of osteoclast precursors and improves the reabsorption function of mature osteoclasts upon binding to its receptor, receptor activator of nuclear factor-κB (RANK) [9]. Furthermore, tumor necrosis factor receptor-associated factor 6 (TRAF6) specifically interacts with the cytoplasmic domain of RANKL when RANKL binds to RANK [10]. This process activates nuclear factor kappa-B (NF-κB) inhibitor kinases (IKKα and IKKβ), which phosphorylate the NF-κB inhibitor IκB at designated serine residues, causing

autoubiquitination and proteasome degradation and thus releasing NF-κB [11]. Activated NF-κB, composed of p50 and p65, is translocated into the nucleus, where it increases the expression of transcription factors, including proto-oncogene protein c-Fos (c-Fos) and nuclear factor of activated T-cells cytoplasmic 1 (NFATc1) [12]. The interaction between c-Fos and NFATc1 promotes the transcription of osteoclast-specific genes, thereby enhancing osteoclast differentiation and activity [13].

The NF-κB signaling pathway plays a core regulatory role in osteoclastogenesis. Studies indicate that activated NF-κB is crucial for osteoclast differentiation and function, promoting their formation by regulating the expression of key transcription factors, such as c-Fos and NFATc1 [14]. RANKL activates both classical and non-classical NF-κB pathways through signaling molecules such as TRAF6, thereby inducing the differentiation of osteoclast precursor cells [15,16]. Additionally, NF-κB enhances osteoclastogenesis by inhibiting its negative regulators, such as interferon regulatory factor 8 (IRF8) and recombination signal binding protein for immunoglobulin kappa J region (RBP-J) [17]. Furthermore, abnormal activation of the NF-κB pathway has been strongly linked to the pathogenesis of various bone-related diseases, including osteoporosis and osteoarthritis, suggesting that inhibiting this pathway could serve as a promising therapeutic strategy. For example, transcriptional co-activator with PDZ-binding motif (TAZ) significantly reduces osteoclast formation by downregulating the transforming growth factor-β-activated kinase 1 (TAK1)/NF-κB signaling pathway [16]. Moreover, natural products such as quercetin and kaempferol exhibit potential inhibitory effects on osteoclastogenesis by targeting the NF-κB signaling pathway [18]. Collectively, these findings suggest that modulating the NF-κB pathway could provide a new approach for preventing and treating osteoclast-mediated diseases.

However, current research on the molecular mechanisms by which sodium hydrosulfide (NaHS) regulates the NF-κB pathway remains limited. To identify potential therapeutic agents for osteoporosis, several chemicals affecting the NF-κB pathway have been investigated, including NaHS. NaHS acts as a donor of hydrogen sulfide (H_2S), a gaseous signaling molecule known as a third major endogenous gasotransmitter [19]. Traditionally regarded as harmful, H_2S is now recognized to play a crucial role in maintaining tissue and organ homeostasis [20,21]. Recent studies have reported that H_2S ide alleviates bone loss in ovariectomized rats by inhibiting the NF-κB signaling pathway [22–25]. Moreover, H_2S has been introduced into injectable hydrogels to guide the balance between immune responses and osteoclastogenesis, offering a novel treatment strategy for osteoporosis [26].

Despite these promising outcomes, the precise functions and underlying mechanisms of H_2S in bone metabolism remain poorly explored. Therefore, the present study aims to investigate and elucidate the specific role of NaHS in osteoporosis and its underlying molecular mechanisms in disease pathogenesis.

Materials and Methods

Cells

Bone marrow-derived macrophages (BMMs) were isolated from the femur and tibia of 6–8-week-old C57BL/6 mice. To ensure reproducibility throughout the experiment, cells were resuspended at a ratio of 1 mouse per 10 mL of medium followed by incubation in 10 cm dishes, and a total of 15 mice were used for BMM isolation. Mice were euthanized by carbon dioxide asphyxiation and disinfected by soaking in 75% ethanol for 10 minutes. Under aseptic conditions in a laminar flow hood, the femur and tibia were harvested from the lower limbs and washed with phosphate-buffered saline (PBS). Briefly, both ends of each bone (femur or tibia) were cut open, and the periosteum and attached tissues were gently eliminated. The bone marrow was carefully flushed out by inserting a 1 mL syringe filled with alpha minimal essential medium (α-MEM) into one end of the bone and rinsing the bone marrow cavity three times until the bone turned white. The collected marrow suspension was centrifuged at 1000 rpm at room temperature for 15 minutes. The resulting supernatant was discarded, and the cell pellet was resuspended in complete α-MEM medium (10% fetal bovine serum supplemented with penicillin/streptomycin) and then seeded into two 10 cm cell culture dishes. Finally, the cells were incubated at 37 °C under humidified conditions of 5% CO_2 for 12–24 hours.

The next day, the cell supernatant and non-adherent cells were discarded. Semi-adherent cells were carefully dislodged from the bottom of the cell culture dish using a 1000 µL pipette, and the cell suspension was then collected. Following centrifugation at 1000 rpm at room temperature for 5 minutes, the supernatant was discarded, and the cell pellet was resuspended in complete α-MEM medium containing 30 ng/mL macrophage-colony stimulating factor (M-CSF). The cells then underwent an additional 12–24-hour incubation until the majority had adhered. As shown in **Supplementary Fig. 1**, the identity of cultured BMMs was verified by flow cytometry using surface marker detection (CD11b+ and F4/80+). The antibodies utilized in flow cytometry were as follows: CD11b (101206, BioLegend, San Diego, CA, USA) and F4/80 (12-4801-82, Invitrogen, Carlsbad, CA, USA).

Additionally, RAW264.7 cells, a mouse macrophage cell line, were purchased from the Cell Bank of the Chinese Academy of Sciences (SCSP-5034, Shanghai, China). Cell line was authenticated using short tandem repeat (STR) profiling (results provided in **Supplementary material 1**), and mycoplasma contamination was routinely evaluated every 2–3 months using a polymerase chain reaction (PCR)-based

mycoplasma detection kit (Lonza MycoAlert™, LT07-318, Lonza Group Ltd., Basel, Switzerland).

Cell Viability Assay

BMMs were seeded into 96-well plates (2×10^4 cells/well) in 100 µL of complete culture medium (α-MEM supplemented with 10% fetal bovine serum and 1% antibiotics). The plates were gently shaken to ensure uniform cell distribution and then incubated at 37 °C with 5% CO_2 for 24 hours allowing the cells to adhere and stabilize. Fresh NaHS solutions were prepared at different concentrations according to the experimental design to prevent NaHS decomposition. The culture medium was removed and 100 µL of medium containing the designated NaHS concentrations was added to each well. For the control group, an equal volume of medium without NaHS was added. Cells were then incubated for an additional 24 hours under the same conditions.

After treatment, 10 µL of cell counting kit-8 (CCK-8) reagent (SB-CCK8-1000ml, Share-bio, Shanghai, China) was added directly to each well without replacing the medium. Plates were gently agitated to ensure thorough mixing, while avoiding bubble formation, which could interfere with absorbance measurements. The culture plates were then incubated at 37 °C with 5% CO_2 for 2 hours in the dark. Subsequently, absorbance (OD) was measured at 450 nm using an Infinite M200 Pro NanoQuant microplate reader (Tecan Group Ltd., Männedorf, Switzerland). Wells containing only medium and CCK-8 (without cells) were included as blanks for background correction. Cell viability was calculated using the following formula: Cell Viability (%) = $\frac{A_{sample} - A_{blank}}{A_{control} - A_{blank}} \times 100\%$. Concentration-response curves were generated, and the half-maximal inhibitory concentration (IC_{50}) was determined through fitting.

Osteoclastogenesis and TRAP Staining

Bone marrow-derived macrophages were seeded in 48-well plates (3×10^4 cells/well) and cultured with 50 ng/mL RANKL (462-TEC, R&D Systems, Minneapolis, MN, USA) and 30 ng/mL M-CSF (416-ML, R&D Systems, Minneapolis, MN, USA) to induce osteoclast differentiation [27].

On day 8 following induction, cells were subjected to tartrate-resistant acid phosphatase (TRAP) staining (387A, Sigma-Aldrich, St. Louis, MO, USA). Briefly, the culture medium was carefully removed, and cells were washed twice with PBS. The cells were then fixed with 4% paraformaldehyde (PFA) at room temperature for 10 minutes, followed two additional PBS washes. The TRAP staining solution was prepared following the manufacturer's instructions by mixing the substrate solution (naphthol AS-BI phosphate) with the chromogenic reagent (Fast Red Violet LB salt) and adding 0.1 M citrate-acetic acid buffer to inhibit non-specific acid phosphatase activity. The staining solution was then added to each well (500 µL for a 6-well plate; 200 µL for a 24-well plate), followed by incubation at 37 °C for 30–60 minutes in the dark.

Following incubation, the staining solution was removed, and cells were washed twice with PBS. TRAP-positive cells, which appear red or purple-red and are typically multinucleated, were observed under an optical microscope. Quantification was conducted by counting the number of TRAP-positive multinucleated cells ($\geq$3 nuclei) and assessing cell morphology and distribution. Semi-quantitative analysis was performed using ImageJ 2.0 software (National Institutes of Health, Bethesda, MD, USA).

Ovariectomy-induced Osteoporosis Model

The ovariectomy (OVX)-induced osteoporosis model was established as described previously [28]. Female C57BL/6J mice (aged 8 weeks and weighing 25–30 g) were purchased from Cyagen Biosciences Inc. (Suzhou, China). All experimental procedures involving animals were performed following institutional ethics guidelines. Mice were randomly divided into 5 groups (n = 6): sham group, OVX group, low-dose NaHS group (0.38 mg/kg); medium-dose NaHS group (0.75 mg/kg), and high-dose NaHS group (1.5 mg/kg). The NaHS doses (0.38, 0.75, and 1.5 mg/kg) were selected based on pilot dose-response experiments and previous reports, which showed that these doses correspond to physiologically achievable plasma H_2S levels in mice without causing toxicity. Control mice received an equal volume of physiological saline instead of NaHS [29,30].

Mice were anesthetized with an intraperitoneal injection of sodium pentobarbital at a dose of 50–70 mg/kg, which provides adequate analgesia meeting the animal ethics requirements. During anesthesia, respiration, heart rate, and body temperature were continuously monitored to ensure experimental stability. Once the mice were fully anesthetized, the dorsal surgical site was shaved and disinfected, and bilateral longitudinal incisions were made near the kidney area. The fascia was carefully incised to separate the muscle and peritoneum, and the ovaries, identifiable as pink tissues attached to the adipocytes, were removed. In the sham group, only a small amount of adipose tissue around the ovary was excised. This strategy ensured that the sham surgery group of mice experienced surgical stress similar to the OVX group, thereby reducing confounding variables such as surgical stress, local tissue damage, and functional effects of fat tissue removal. After excision, wounds were sutured in layers, and gentamicin was applied daily for 3 consecutive days to prevent infection. The excised ovarian tissues were confirmed by preparing frozen sections (6 µm) and hematoxylin and eosin (H&E) staining, which showed the presence of ovarian tissues under the microscope.

Euthanizing Methods and Procedures for Bone Sampling

As per animal ethics guidelines, euthanasia procedures must be rapid, painless, and designed to reduce suffering and unnecessary stress. CO_2 inhalation was applied by placing the mice in a transparent euthanasia chamber and slowly introducing CO_2 at a flow rate of typically 20%–30% of the chamber volume per minute, thereby minimizing stress responses associated with rapid exposure. CO_2 introduction was continued until respiration ceased (usually within 2–5 minutes), followed by an additional one-minute exposure to ensure complete death.

Following euthanasia, mice were placed in the supine position on the surgical table. The entire body, especially the limbs and abdomen, was disinfected with 75% alcohol. A surgical scissor was used to make an incision along the midline of the abdomen, extending posteriorly toward the tail and laterally toward the hind limbs, allowing the skin to be peeled back and the hind limb muscles exposed. Using fine anatomical scissors or a scalpel, muscles covering the femur and tibia were carefully removed, starting at the hip joint and proceeding distally along the femur and tibia, while avoiding bone damage. At the knee joint, the muscles were cut to fully expose both the femur and tibia. For femur collection, the joint ligaments at the hip joint were cut with scissors to separate the femur from the pelvis. The femur was carefully excised without damaging the bone and then washed with PBS to remove residual soft tissues.

For tibia collection, the tibia was separated from the femur by cutting at the knee joint. Surrounding muscles and tendons were carefully separated along the length of the tibia, and the bone was excised intact without damaging its surface, followed by rinsing with PBS to remove residual soft tissues.

Preservation methods were selected based on subsequent experimental requirements. For immediate use, bones were placed in sterile PBS to keep them moist. However, for fixation experiments, skeletal tissues were immersed in 4% paraformaldehyde, while for cryopreservation, bones were frozen in liquid nitrogen and then stored at –80 °C.

Micro-CT Analysis

Femurs or tibias were fixed in 75% of ethanol at 4 °C and scanned using a SkyScan 1176 micro-computed tomography (micro-CT) scanning system (Bruker, Kontich, Belgium). Structural indices were quantified with CTAn 1.16.4.1 software (Bruker, Kontich, Belgium), and a 3D model was generated. The region of interest (ROI) was defined as the area 5 mm below the growth plate. During micro-CT analysis, the following parameters were analyzed: bone mineral density (BMD), bone volume to total volume ratio (BV/TV), bone surface-to-volume ratio (BS/BV), trabecular number (Tb.N), trabecular separation (Tb.Sp), trabecular thickness (Tb.Th), and trabecular pattern factor (Tb.pf).

Bone Histology and Histomorphometry

Mice were sacrificed, and femurs were fixed in 4% paraformaldehyde for 72 hours without decalcification before sectioning. Histological and histomorphometric examinations were performed using H&E staining, TRAP staining, and immunohistochemistry (IHC).

For H&E staining (G1120, Solarbio, Beijing, China), bones underwent a series of preparations, including decalcification, sectioning, and staining. Initially, fixed bone tissues were decalcified in a 10% ethylene diamine tetraacetic acid (EDTA) until they became soft and amenable to sectioning, then embedded in paraffin and cut into 3–5 µm sections. For staining, tissue sections were treated with hematoxylin for 5–10 minutes to stain nuclei (which appear blue), followed by eosin staining for 2–3 minutes to counterstain the cytoplasm and extracellular matrix (pink). Finally, the sections were dehydrated through a graded ethanol, cleared in xylene, and mounted with neutral gum. Histological assessments of bone cells and structure were performed using a Nikon Eclipse TE2000 microscope (Nikon Instruments Inc., Tokyo, Japan).

TRAP staining (387A, Sigma-Aldrich, St. Louis, MO, USA) was utilized to detect tartrate-resistant acid phosphatase activity in osteoclasts. Briefly, fixed bone tissue was sectioned at 3–5 µm thickness and then immersed in TRAP staining solution for 15–30 minutes. During this process, the enzymatic reaction produced a red precipitate, indicating the presence of osteoclasts. After staining, sections were rinsed with distilled water to terminate the reaction, mounted with neutral gum, and observed under a Nikon Eclipse TE2000 microscope to evaluate osteoclast distribution and abundance.

IHC staining was conducted to detect the expression and localization of specific proteins in bone tissue. Fixed bone tissues were sectioned at a thickness of 3–5 µm. Following antigen retrieval, sections were blocked with a blocking buffer for 30 minutes to prevent nonspecific binding. Primary antibodies (anti-IkB-α, 1:200; 4814, Cell Signaling Technology, Danvers, MA, USA) were applied and incubated overnight at 4 °C. The next day, sections were incubated with secondary antibodies (1:200; RK50015, ABclonal, Wuhan, China) at room temperature for 30–60 minutes. Signal detection was performed using 3,3′-diaminobenzidine (DAB) chromogen, with staining intensity monitored under a microscope. The reaction was terminated by rinsing in distilled water. Furthermore, nuclei were counterstained with hematoxylin, and sections were dehydrated in graded ethanol, cleared in xylene, and mounted with neutral gum. The expression and localization of the target proteins were then observed under a Nikon Eclipse TE2000 microscope.

Luciferase Assay

For the dual-luciferase reporter assay, RAW264.7 cells were seeded in 96-well plates at a density of 2×10^4

cells/well (triplicate wells for each condition). After 24 hours, cells were transfected with the p-NF-kB-Luc plasmid (0.1, 0.5, or 1.0 µg/well) along with 0.5 µg Renilla-Luc (internal control) using Lipofectamine 3000 (L3000150, Thermo Fisher Scientific, Waltham, MA, USA). Following 48 hours of incubation, cells were lysed, and absorbance at 480 nm was measured using an Infinite M200 Pro NanoQuant microplate reader (Tecan Group Ltd., Männedorf, Switzerland). The plasmid sequence is given in the **Supplementary material 2**.

Immunofluorescence Assay

BMMs were cultured in confocal culture dishes and treated with 0.15 mM NaHS for 12 hours. Cells were then fixed with 4% paraformaldehyde for 10 minutes and underwent three PBS washes. Subsequently, membrane permeabilization was conducted using 0.25% Triton X-100 for 15 minutes, followed by blocking with 5% bovine serum albumin (BSA) for 1 hour. The cells were then incubated overnight with the primary antibody (anti-p65, Cell Signaling Technology, 8242, 1:200). The next day, cells underwent three PBS washes, followed by a 2-hour incubation with the secondary antibody (1:200; AS073, Cell Signaling Technology, Danvers, MA, USA). Furthermore, nuclei were counterstained with 4′6-diamidino-2-phenylindole (DAPI) (NucBlue™ Fixed Cell ReadyProbes™, R37606, Thermo Fisher Scientific, Waltham, MA, USA) for 5 minutes, and fluorescence intensity and localization were assessed using a laser confocal microscope (FV3000, Olympus Corporation, Tokyo, Japan).

Western Blot Analysis

Total proteins were isolated from cells cultured under standard conditions (37 °C, 5% CO_2). After experimental treatment, cells were lysed using radioimmunoprecipitation assay (RIPA) lysis buffer (20-188, Sigma-Aldrich, St. Louis, MO, USA) containing 1% phenylmethanesulfonyl fluoride (PMSF) (10837091001, Sigma-Aldrich, St. Louis, MO, USA) to extract total proteins.

Protein resolving gels were prepared by mixing 30% acrylamide, Tris-HCl (pH 8.8 or 6.8), 10% ammonium persulfate (APS), 10% sodium dodecyl sulfate (SDS), double-distilled water (ddH_2O), and N,N,N′,N′-tetramethylethylenediamine (TEMED). However, a 10% gel was employed for most proteins, while 8% gel was used for proteins $>$100 kDa and 12% gel for proteins $<$40 kDa. Protein samples were loaded onto the gel, and electrophoresis was performed at 90 V for ~20 minutes, followed by 120 V until the lowest marker approached the bottom. Subsequently, proteins were transferred onto a polyvinylidene fluoride (PVDF) membrane using a wet transfer system at 200 mA, with time adjusted according to protein size. Membranes were then blocked in 5% skim milk for 2 hours at room temperature (5% BSA was used for phosphorylated proteins).

Membranes were incubated overnight at 4 °C with primary antibodies, diluted in TBS with Tween-20 (TBST) following the manufacturer's instructions, with gentle agitation. The next day, membranes were washed three times with TBST (10 minutes each wash) and incubated with species-specific horseradish peroxidase (HRP)-conjugated secondary antibody (1:10,000 in TBST) at room temperature for 1 hour. Following three washes with TBST (10 minutes each wash), protein bands were visualized using the ECL system and images were captured with the Tanon 5200 Multi Chemiluminescent Imaging System (Tanon Science & Technology Co., Ltd., Shanghai, China).

Grayscale value of the protein bands was quantified using ImageJ 2.0 software. Raw western blot images were uniformly sized, and rectangular boxes were manually drawn around each target band, and the corresponding internal reference band included the entire band area. The software automatically calculated the integrated optical density (IOD) values for each band, or area density (AD) values of pixels within each selected rectangular box, representing the total grayscale value of the band. For normalization, the ratio of the target protein band intensity (IOD_Target) to the corresponding internal reference protein band intensity (IOD_LoadingControl) was calculated for each band. Relative protein expression was evaluated by comparing these normalized ratios to the average ratio of the control group (set to 1), and fold changes in protein expression were calculated accordingly. Quantitative data were acquired from at least 3 independent biological replicates and expressed as Mean $\pm$ SEM (or SD).

The following antibodies were used in western blot analysis: anti-NFATc1 (1:1000; 8032, Cell Signaling Technology); anti-c-Fos (1:1000; 2250, Cell Signaling Technology); anti-p65 (1:1000; 8242, Cell Signaling Technology); anti-histone H3 (1:1000; 4499, Cell Signaling Technology); anti-IκB-α (1:1000; 4814, Cell Signaling Technology); anti-phospho-IκB-α (1:1000; 2859, Cell Signaling Technology); anti-IKKα (1:1000; 61294, Cell Signaling Technology); anti-IKKβ (1:1000; 8943, Cell Signaling Technology); anti-Phospho-IKK-α/β (1:1000; 1023, Cell Signaling Technology); anti-p100/p52 (1:1000; 4882, Cell Signaling Technology); anti-ubiquitin (1:1000; 58395, Cell Signaling Technology); anti-ERK (1:1000; 4695T, Cell Signaling Technology); anti-p-ERK (1:1000; 4370, Cell Signaling Technology); anti-JNK (1:1000; 67096, Cell Signaling Technology); anti-p-JNK (1:1000; 4668, Cell Signaling Technology); anti-p38 (1:1000; 8690, Cell Signaling Technology); anti-p-p38 (1:1000; 4511, Cell Signaling Technology); anti-β-actin (1:3000; 4970, Cell Signaling Technology), and HRP-conjugated secondary antibodies (1:5000; anti-rabbit IgG: BA1055, anti-mouse IgG: BA1050, Boster).

Table 1. Primers used in qRT-PCR.

Genes	Forward primer	Reverse primer
GAPDH	ACCCAGAAGACTGTGGATGG	CACATTGGGGGTAGGAACAC
CTSK	CTTCCAATACGTGCAGCAGA	TCTTCAGGGCTTTCTCGTTC
TRAP	CTGGAGTGCACGATGCCAGCGACA	TCCGTGCTCGGCGATGGACCAGA
V-ATPase d2	AAGCCTTTGTTTGACGCTGT	TTCGATGCCTCTGTGAGATG

qRT-PCR, quantitative real-time polymerase chain reaction; *GAPDH*, glyceraldehyde 3-phosphate dehydrogenase; *TRAP*, tartrate-resistant acid phosphatase; *CTSK*, cathepsin K; *V-ATPase d2*, v-type proton ATPase subunit d2.

Quantitative Real-time PCR Analysis

Total RNA was isolated from BMMs following the guidelines provided by the manufacturer. The extracted RNA was subsequently converted into cDNA through reverse transcription. Using cDNA as a template, quantitative real-time PCR (qRT-PCR) was performed on an Applied Biosystems 7500 Real-Time PCR System (Thermo Fisher Scientific, Waltham, MA, USA). Glyceraldehyde 3-phosphate dehydrogenase (GAPDH) was used as the internal control, and relative gene expression levels were determined using the $2^{-\Delta\Delta Ct}$ method. The primers used in qRT-PCR are listed in Table 1.

Flow Cytometry

BMMs were exposed to NaHS at varying concentrations (0, 0.3, 0.6, or 2.4 µM) for 48 hours, then resuspended in binding buffer and stained with Annexin V-FITC and PI (SB-F6012, Share-bio, Shanghai, China) for 15 minutes. Moreover, apoptosis was evaluated using a FACS Canto II (BD) by acquiring signals from 10,000 cells excited at 488 nm, with emission obtained at 585/42 (564–606 nm) and 702/64 (670–735 nm). Results were analyzed using FACSDiva 8.01 software (BD Biosciences, San Jose, CA, USA), and the proportion of apoptotic cells was determined for each treatment group.

Statistical Analysis

Statistical analysis was conducted using SPSS 20.0 software (IBM Corp., Armonk, NY, USA). Data were analyzed using Student's unpaired *t*-tests or one-way analysis of variance (ANOVA), as appropriate. Post hoc pairwise comparisons were performed using Tukey's honestly significant difference (HSD) test to identify specific group differences. A *p*-value of less than 0.05 was considered statistically significant.

Bioinformatics Analysis of Transcriptomic Data

BMMs were treated with a mycoplasma removal reagent and expanded into six 10 cm culture dishes to generate biological replicates per group. Upon reaching 80%–90% confluency, the control group was left untreated, while the experimental group was treated with 0.15 mM NaHS for 0.5 hours. Total RNA was then extracted using the Trizol reagent, and transcriptome sequencing was conducted.

For differential expression analysis, RNA sequencing (RNA-seq) data were analyzed using the DESeq2 package. The fold change and *p*-values of gene expression were visualized in a volcano plot, with fold changes and *p*-values transformed by log2 and –log10, respectively. Gene Ontology (GO) enrichment of differentially expressed genes (DEGs) was performed using the ClusterProfiler package, detecting significantly enriched biological processes, molecular functions, and cellular components (*p*. adjust < 0.05). Similarly, Kyoto Encyclopedia of Genes and Genomes (KEGG) pathway enrichment analysis of DEGs was also conducted using ClusterProfiler, with significantly enriched pathways ranked according to adjusted *p*-values. Furthermore, during biocarta pathway analysis, gene sets were annotated using the MSigDB database, followed by enrichment analysis with ClusterProfiler. Moreover, gene set enrichment analysis (GSEA) was performed using a ranked gene list, based on log2 fold change, $|\log FC| > 1$. Normalized enrichment scores (NES) and *p*-values were calculated, and significant results were visualized as enrichment plots. Finally, data visualization was conducted with the R package ggplot2 for volcano plots, bar charts, and bubble plots, while GSEA plots were generated using the built-in functions of ClusterProfiler.

Results

NaHS Inhibits RANKL-Induced Osteoclastogenesis In Vitro

To determine the cytotoxicity of NaHS in BMMs, cell viability was assessed using the CCK-8 assay at 48 and 96 hours. At 48 hours, 0.30 mM NaHS showed no significant toxicity ($p > 0.05$; Fig. 1A). A 96-hour, the IC_{50} of NaHS was found to be 0.88 ± 0.01 mM (Fig. 1B). *In vitro* assays further confirmed that NaHS at concentrations of 0.05 and 0.10 mM did not induce apoptosis in BMMs ($p > 0.05$; **Supplementary Fig. 2A,B**). Hence, these concentrations were selected for subsequent osteoclast induction assays. Nine experimental groups were established to examine the effects of NaHS on osteoclast differentiation in BMMs. Analysis revealed that the average number of TRAP+ multinucleated osteoclasts was 14 cells per microscopic field in the control group. However, NaHS treatment suppressed osteoclast formation in a concentration-

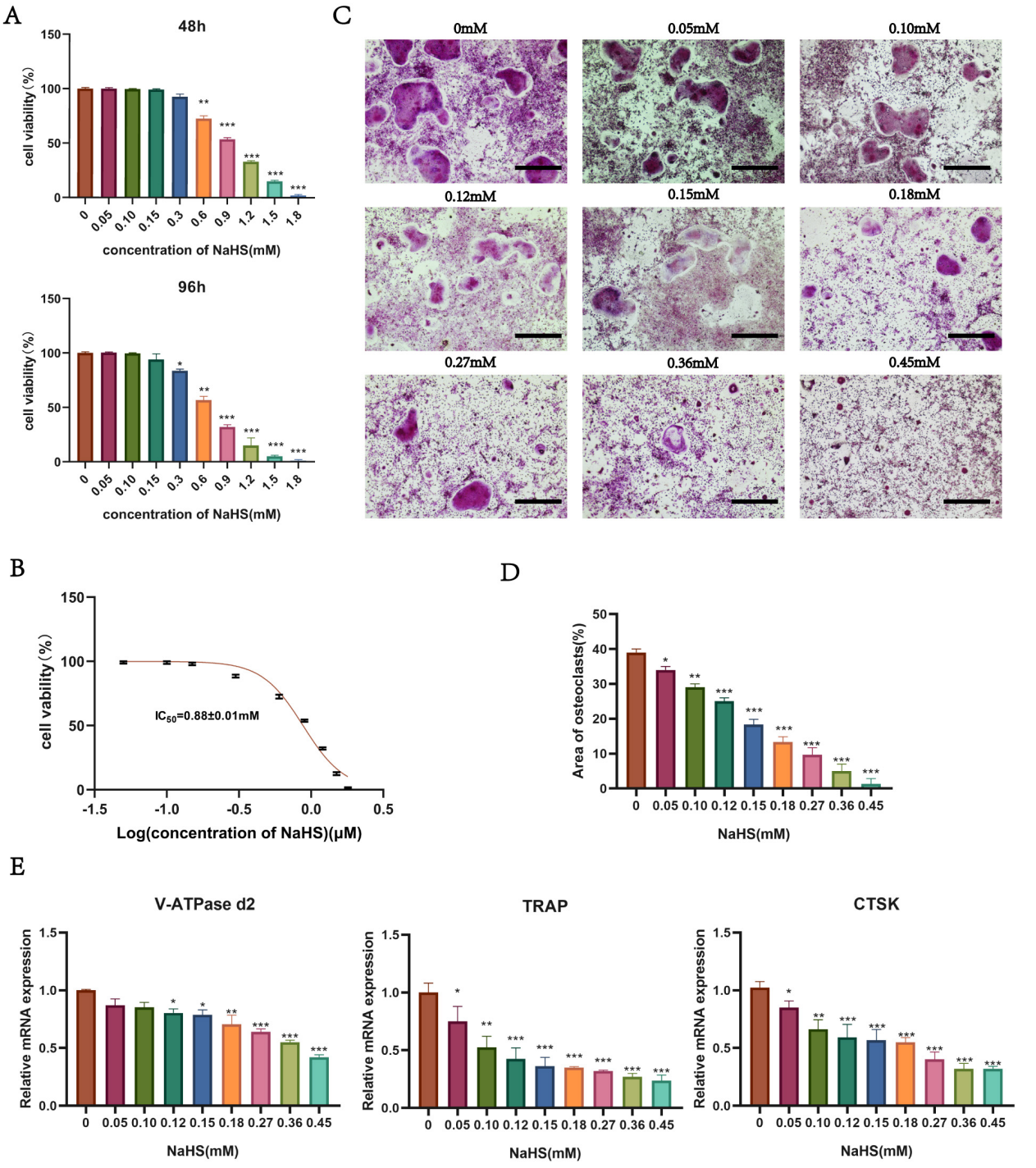

Fig. 1. Sodium hydrosulfide (NaHS) regulates osteoclastogenesis in a time- and dose-dependent manner. (A) Effects of NaHS on bone marrow-derived macrophage (BMM) viability at 48 and 96 hours. (B) Half-maximal inhibitory concentration (IC_{50}) values of NaHS against BMMs. (C) Tartrate-resistant acid phosphatase (TRAP)-positive BMMs treated with different NaHS concentrations followed by stimulation with M-CSF and receptor activator of nuclear factor-κB ligand (RANKL) for 7 days. (D) Quantification of TRAP-positive cell distribution and osteoclast localization. (E) The expression levels of osteoclast-related markers (V-ATPase d2, TRAP, and CTSK) in BMMs were treated with designated NaHS concentrations for 7 days. All experiments were performed at least three times. Scale bar = 100 μm. *$p < 0.05$, **$p < 0.01$, ***$p < 0.005$, compared to the untreated cells. V-ATPase d2, v-type proton ATPase subunit d2; M-CSF, macrophage-colony stimulating factor; CTSK, cathepsin K.

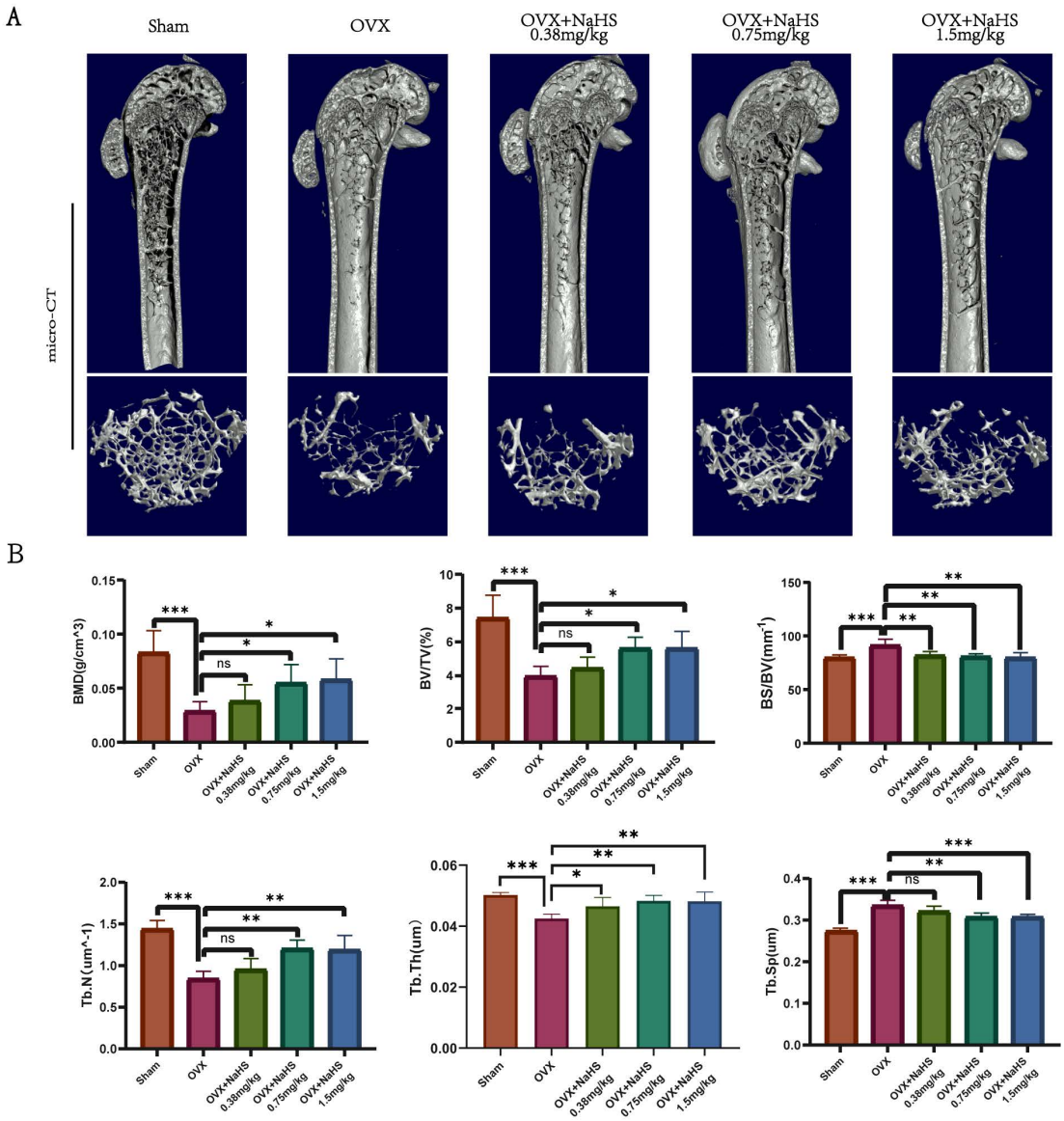

Fig. 2. NaHS treatment prevents ovariectomized (OVX)-induced bone loss *in vivo*. (A) The femurs of sham mice and OVX mice treated with NaHS for 4 weeks were analyzed by micro-CT, and three-dimensional reconstructions are presented. (B) Bone mineral density (BMD), bone volume to total volume ratio (BV/TV), bone surface-to-volume ratio (BS/BV), trabecular thickness (Tb.Th), trabecular number (Tb.N), and trabecular separation (Tb.Sp) analysis in all five experimental groups. n = 6, *$p < 0.05$, **$p < 0.01$, ***$p < 0.005$. ns, not significant; micro-CT, micro-computed tomography.

dependent manner, and at 0.45 mM NaHS concentration, osteoclastogenesis was almost completely abolished ($p < 0.005$; Fig. 1C,D).

To further clarify the inhibitory effect of NaHS at the molecular level, the expression of osteoclast-related genes was evaluated under different NaHS concentrations. The expression levels of v-type proton ATPase subunit d2 (V-ATPase d2), tartrate-resistant acid phosphatase (TRAP), and cathepsin K (CTSK) were substantially decreased in a dose-dependent manner ($p < 0.05$; Fig. 1E), suggesting suppression of osteoclastogenesis.

Collectively, these results indicate that NaHS significantly inhibits the differentiation and growth of osteoclasts, both at the cellular and transcriptional levels. While low concentrations of NaHS exhibit no significant cytotoxicity in BMMs, high concentrations exert considerable inhibitory effects. Meanwhile, based on these results, 0.15 mM was selected as a safe and effective concentration for subsequent *in vitro*, mechanistic experiments.

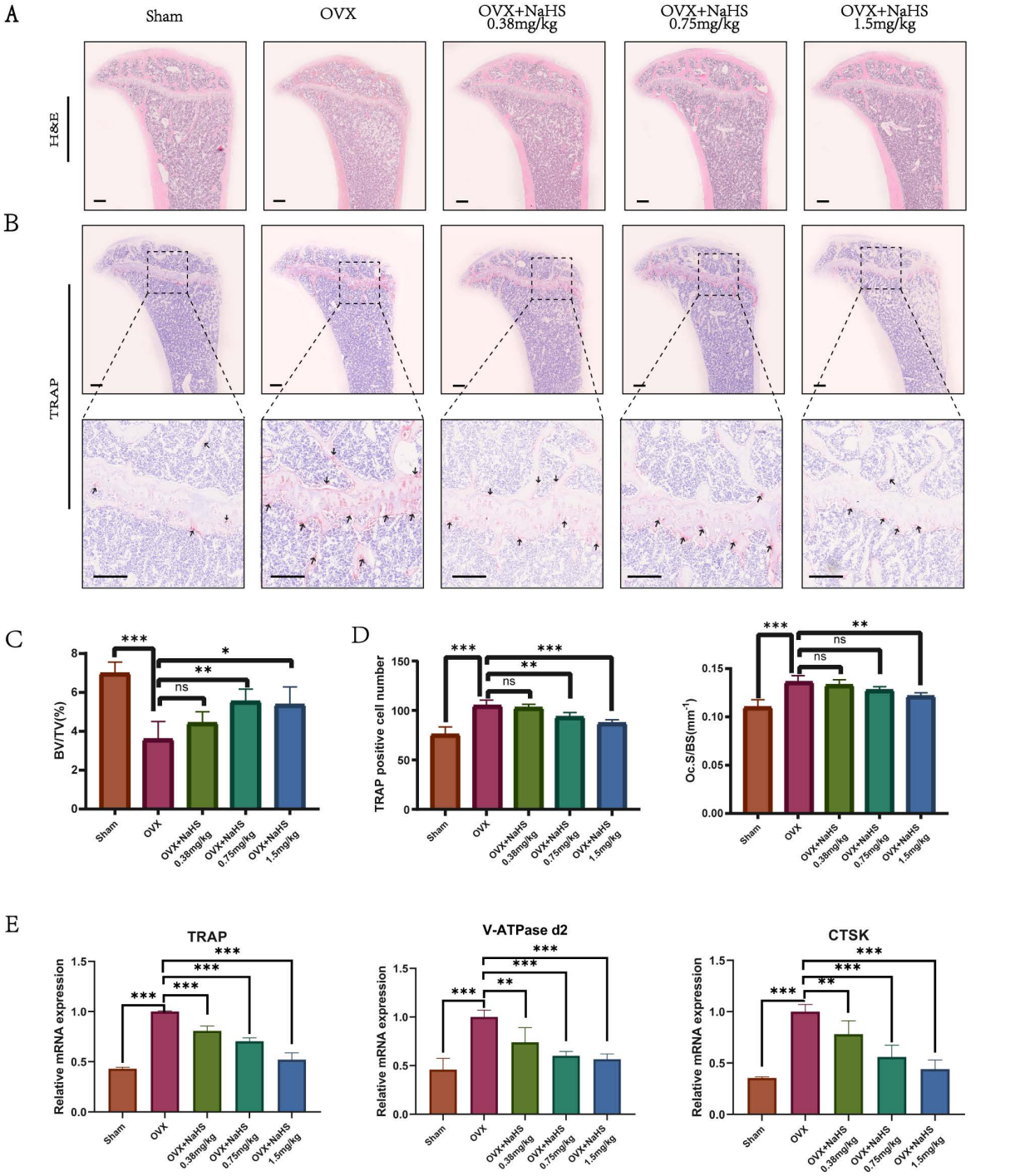

Fig. 3. NaHS alleviates OVX-induced osteoporosis by inhibiting osteoclast formation. (A,B) Hematoxylin and eosin (H&E) (magnification ×25) and TRAP (magnification ×25/100) staining of the vertebral body sections, black arrows indicate TRAP+ cells. (C) BV/TV assessed through H&E staining. (D) Number of TRAP-positive cells and osteoclast-to-bone surface area ratio (Oc.S/BS)%. (E) The expression of osteoclast markers (V-ATPase d2, TRAP, and CTSK) in five experimental groups. Scale bars = 100 µm. n = 6, $*p < 0.05$, $**p < 0.01$, $***p < 0.005$.

NaHS Attenuates OVX-Induced Osteoporosis In Vivo

A mouse model of OVX-induced osteoporosis was successfully established to assess the therapeutic effect of NaHS. Briefly, 8-week-old OVX mice were treated with varying concentrations of NaHS (low: 0.38 mg/kg; medium: 0.75 mg/kg; high: 1.5 mg/kg) for 4 weeks. Femurs were then analyzed by micro-CT to generate 3D reconstructions and perform histomorphometric analyses (Fig. 2A).

As shown in Fig. 2B, compared to the Sham group, the OVX group exhibited a significant bone loss, as evidenced by a reduction in BMD, BV/TV, Tb.Th, and Tb.N ($p < 0.05$). In contrast, Tb.Sp ($p < 0.05$) and BS/BV were significantly elevated in the OVX group ($p < 0.05$). Furthermore, NaHS treatment effectively reversed these changes in a dose-dependent manner. Notably, the OVX+NaHS group (1.5 mg/kg) demonstrated a significant increase in BMD compared to the OVX group ($p < 0.05$). Similarly, BV/TV, Tb.Th, and Tb.N were substantially elevated, whereas Tb.Sp and BS/BV values were reduced ($p < 0.05$ vs. OVX).

These findings suggest that NaHS protects against OVX-induced bone loss. The increases in BMD, BV/TV, Tb.Th, and Tb.N indicate enhanced bone formation and improved trabecular microstructure, while the decreases in Tb.Sp and BS/BV suggest inhibition of bone resorption. These findings are consistent with previous studies showing that NaHS regulates bone metabolism by affecting osteoblast and osteoclast activity. The dose-dependent effect of NaHS further highlights its potential as a therapeutic agent for osteoporosis. Furthermore, assessment of potential systemic toxicity showed no substantial histopathological changes in the liver or kidneys of mice treated with low, medium, or high concentrations of NaHS for four weeks (**Supplementary Fig. 3**), confirming its safety at the designated dose *in vivo*.

NaHS Attenuates OVX-Induced Osteoporosis by Suppressing Osteoclastogenesis

Bone metabolism is a dynamic process involving osteoblast-mediated bone formation and osteoclast-mediated bone resorption. While micro-CT scanning confirmed that NaSH elevated bone density and trabecular number in OVX mice in a concentration-dependent manner, it remained unclear whether this effect was due to enhanced osteoblast activity or inhibited osteoclast function. Therefore, to address this challenge, undecalcified tibial sections were histologically analyzed after four weeks of NaHS treatment.

Histological staining revealed that NaHS significantly mitigated OVX-induced bone loss, consistent with the results from micro-CT. H&E staining (Fig. 3A) showed a substantial reduction in trabecular bone density in the OVX group compared to the Sham group. TRAP staining (Fig. 3B) indicated a considerable increase in the number of multinucleated osteoclasts in the OVX group. Similarly, NaHS treatment restored BV/TV values ($p < 0.05$ vs. OVX; Fig. 3C), reduced osteoclast numbers ($p < 0.05$ vs. OVX; Fig. 3D), and substantially alleviated the osteoclast-to-bone surface area ratio (Oc.S/BS; $p < 0.05$; Fig. 3D).

Gene expression analysis further confirmed these outcomes (Fig. 3E). OVX substantially upregulated osteoclastogenesis markers, including TRAP, V-ATPase d2, and CTSK ($p < 0.05$ vs. Sham). However, NaHS treatment potentially suppressed the expression of these markers in a dose-dependent manner, with profound reduction found in the medium- and high-dose groups ($p < 0.05$ vs. OVX).

Collectively, these findings suggest that NaHS protects against OVX-induced bone loss primarily by inhibiting osteoclastogenesis. The dose-dependent effects highlight NaHS as a potential therapeutic agent for osteoporosis by modulating bone remodeling.

NaHS Suppresses Osteoclastogenesis by Inhibiting the NF-κB Pathway

To further elucidate the molecular mechanisms by which NaHS inhibits osteoclast differentiation, transcriptome sequencing was performed. DEGs (those upregulated and downregulated) were identified between the NaHS-treated and control groups and visualized in a volcano plot (Fig. 4A), revealing the distribution of significantly upregulated and downregulated genes. Among them, Tcf7l1 and Bhmt1b were significantly upregulated, while Nfkb1 and Traf3 were substantially downregulated, suggesting that these genes may play crucial regulatory roles in the observed biological effects.

Furthermore, functional enrichment analysis of DEGs was performed to investigate their functional implications. The GO analysis (Fig. 4B) indicated that downregulated DEGs were significantly enriched in biological processes, including the NF-κB signaling pathway and ubiquitin protein ligase activity, suggesting that these genes may exert their functions through these mechanisms. Additionally, KEGG pathway analysis (Fig. 4C) similarly found significant enrichment of the NF-κB signaling pathway among the downregulated DEGs. Moreover, GSEA analysis was then performed with a focus on the NF-κB pathway (Fig. 4D,E). The BIOCARTA_NFKB_PATHWAY gene set was observed to be significantly inhibited, indicating that NF-κB signaling was suppressed following treatment with 0.15 mM NaHS for 0.5 hours.

To further elucidate the molecular mechanism by which NaHS suppresses osteoclast formation, common signaling pathways mediating osteoclast differentiation were examined. The expression and phosphorylation levels of c-Jun N-terminal kinase (JNK), extracellular signal–regulated kinase (ERK), and p38, key components of the mitogen-activated protein kinase (MAPK) pathway, were evaluated in both the control and NaHS-treated groups. NaHS did not alter the phosphorylation levels of these molecules, indicating that its inhibitory effect on osteoclast formation is not mediated through MAPK signaling (**Supplementary Fig. 4**). Furthermore, the expression levels of c-Fos and NFATc1, key downstream molecules of the NF-κB pathway, were also evaluated. Analysis revealed that treatment with 0.15 mM NaHS substantially alleviated c-Fos and NFATc1 expression during osteoclast differentiation ($p < 0.005$; Fig. 5A), with an evident concentration-dependent effect observed ($p < 0.005$; Fig. 5B). More-

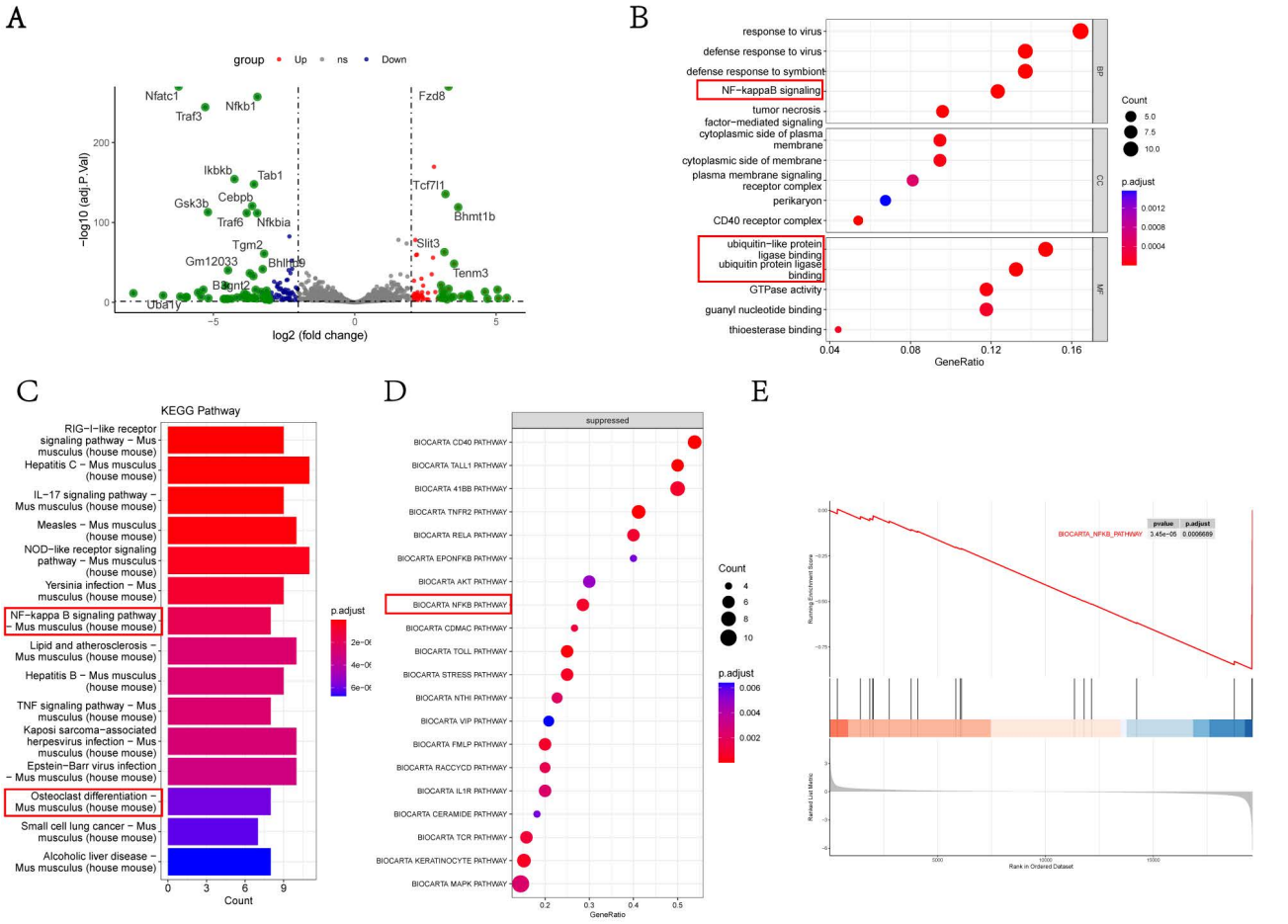

Fig. 4. Transcriptome analysis of differentially expressed genes (DEGs) and their functional enrichment analysis in the NaHS-treated and control groups. (A) The volcano plot illustrates the distribution of DEGs. The x-axis represents log2 fold change, and the y-axis represents –log10 transformed *p*-values. Green color indicates the most significantly changed genes. Red, blue, and gray colors indicate upregulated, downregulated, and non-significant genes, respectively. Some significantly distinct genes are labeled. (B) Gene Ontology (GO) functional enrichment analysis results show significantly enriched biological processes, molecular functions, and cellular components, with a focus on the NF-κB signaling pathway and ubiquitin ligase-related functions. (C) Kyoto Encyclopedia of Genes and Genomes (KEGG) pathway analysis presents significantly enriched signaling pathways, including the RIG-I-like receptor signaling pathway and the NF-κB signaling pathway. Pathways are sorted by significance, with darker colors indicating smaller adjusted *p*-values. (D) Biocarta pathway enrichment analysis displays significantly enriched pathways under suppressive conditions, where NF-κB-related pathways are significantly inhibited. (E) Gene set enrichment analysis (GSEA) results highlight the inhibition trend of the Biocarta NF-κB pathway in gene ranking, indicating significant *p*-values with a negative normalized enrichment score (NES). The red boxes represent the pathways or biological processes with the most significant changes. NF-κB, nuclear factor kappa-B; CD40, cluster of differentiation 40; GTPase, guanosine triphosphatase; RIG-I, retinoic acid-inducible gene I; IL-17, interleukin-17; NOD, nucleotide-binding oligomerization domain; TNF, tumor necrosis factor.

over, luciferase reporter assays showed that NaHS effectively suppressed the transcriptional activity of NF-κB ($p < 0.05$; Fig. 5C). These findings suggest that NaHS suppresses osteoclast formation primarily by inhibiting NF-κB signaling rather than MAPK pathways.

Furthermore, to assess whether NaHS affects NF-κB activation, immunofluorescence assay and western blotting were performed to investigate the nuclear translocation of p65, a core molecule of NF-κB pathway. The results demonstrated that NaHS significantly inhibited p65 nuclear translocation ($p < 0.005$; Fig. 5D,E). Previous studies have shown that RANKL stimulation promotes phosphorylation of IκB-α, resulting in its ubiquitination degradation [31]. Our findings confirmed this phenomenon and notably showed that NaHS inhibited RANKL ($p < 0.05$; Fig. 5F) and also suppressed the phosphorylation of IKK-α/β ($p < 0.05$; Fig. 5G,H).

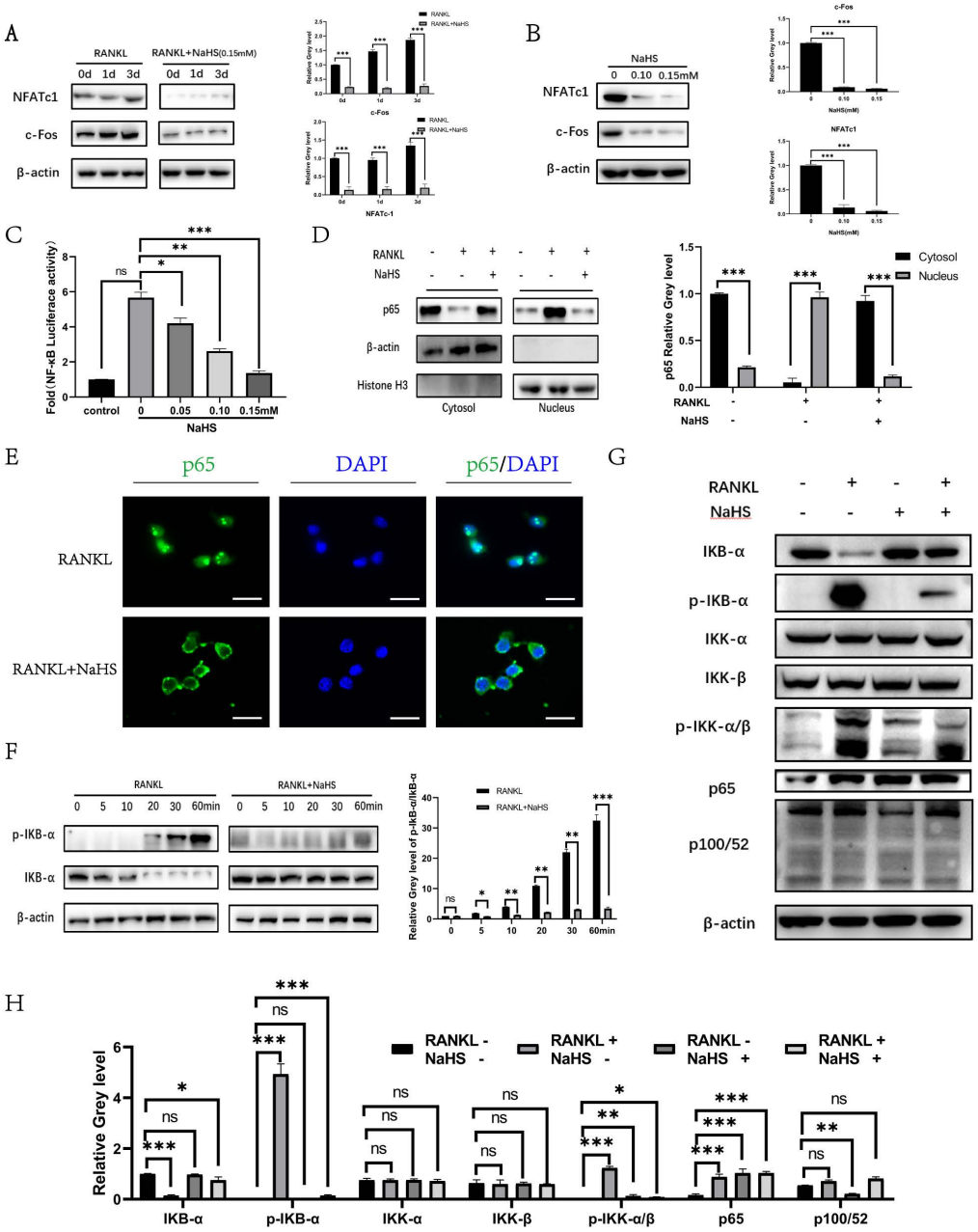

Fig. 5. NaHS suppresses osteoclastogenesis by mediating the phosphorylation of IkB-α and inhibiting NF-κB nuclear translocation. (A) NFATc1 and c-Fos expression levels in BMMs treated with NaHS for 0, 1, and 3 days. Untreated cells served as the control. (B) NFATc1 and c-Fos expression levels in BMMs treated with different concentrations of NaHS (0, 0.10 and 0.15 mM). (C) NF-κB–luciferase reporter gene expression in RAW264.7 cells. The results were normalized to renilla luciferase expression and are expressed as a fold change relative to the control levels. (D) Cells were pretreated with 0.15 mM NaHS for 2 hours before the stimulation with RANKL for 30 minutes. The levels of p65 in the nucleus and cytoplasm after nucleo-cytoplasmic separation were detected using western blotting. (E) Cells were pretreated with 0.15 mM NaHS for 2 hours before the stimulation with RANKL for 30 minutes. Nuclear translocation of p65 was visualized using immunofluorescence (Scale bars = 10 μm). (F) RAW264.7 cells were pretreated with 0.15 mM NaHS for 2 hours before the addition of RANKL, and the levels of p-IκB-α/IκB-α were determined. (G) Expression levels of the indicated proteins in RAW264.7 cells. (H) Relative gray level of the indicated proteins in RAW264.7 cells. *$p < 0.05$, **$p < 0.01$, ***$p < 0.005$. The "+" indicates the presence of this substance, while the "-" indicates the absence of this substance. DAPI, 4′6-diamidino-2-phenylindole; IκB-α, inhibitor of NF-κB alpha; p-IκB-α, phosphorylated IκB-α; IKKα, inhibitor of nuclear factor κB kinase subunit alpha; IKKβ, inhibitor of NF-κB kinase subunit beta; p-IKK-α/β, phosphorylated IKKα/β; NFATc1, nuclear factor of activated T-cells cytoplasmic 1; c-Fos, proto-oncogene protein c-Fos; p65, transcription factor p65; p100/52, nuclear factor NF-kappa B p100/52 subunit.

NaHS Inhibits the Ubiquitination and Degradation of IκB-α

GO analysis showed that downregulated genes were significantly enriched after NaHS treatment in biological processes related to the NF-κB pathway and protein ubiquitination. Therefore, we hypothesized that NaHS may affect the ubiquitination process within the NF-κB pathway, particularly the ubiquitination and degradation of IκB-α.

Immunohistochemical staining revealed that the expression level of IκB-α was significantly decreased in OVX mice ($p < 0.005$; Fig. 6A,B). Notably, NaHS treatment restored IκB-α levels in a dose-dependent manner ($p < 0.01$ vs. OVX).

Western blot analysis further confirmed these findings, demonstrating that the protein level of IκB-α was significantly increased after treatment with MG132, a specific inhibitor of the ubiquitin proteasome system. However, NaHS further enhanced this effect ($p < 0.01$; Fig. 6C). Consistently, ubiquitination assays revealed that NaHS inhibited the ubiquitination of IκB-α, as evidenced by a substantial reduction in ubiquitinated IκB-α band intensity (Fig. 6E), indicating that NaHS interferes with the ubiquitination process.

Additionally, both the number and area of TRAP-positive osteoclasts were significantly decreased when MG132 and NaHS were added simultaneously during RANKL-induced osteoclast differentiation ($p < 0.05$, Fig. 6D,F,G). These results suggest that NaHS protects against OVX-induced bone loss by inhibiting the ubiquitination and degradation of IκB-α, thereby modulating the NF-κB pathway.

Furthermore, immunohistochemical staining of tibia tissue slices showed that, compared to the OVX group, NaHS (0.75 mg/kg) significantly decreased the phosphorylation of IkB-α, while increasing IkB-α protein levels and reducing p65 nuclear translocation ($p < 0.05$; Fig. 7A–C). These results indicate that NaHS suppresses osteoclastogenesis by inhibiting the ubiquitination and degradation of IκB-α, thereby downregulating NF-κB pathway activation.

Discussion

Although substantial advances have been made in the treatment of osteoporosis over the past decades, alternative therapeutic approaches are still required. Current treatment options for osteoporosis include anti-resorptive agents such as bisphosphonates, estrogen replacement therapy, and RANKL inhibitors; however, each of these strategies has significant limitations [32,33]. Therefore, drug development for osteoporosis remains a primary research focus, especially approaches aimed at inhibiting osteoclast formation [34]. In this study, we found that NaHS inhibits osteoclast formation and ameliorates osteoporosis by targeting the NF-κB signaling pathway.

NaHS, a catabolic regulator, inhibits osteoclast formation and function in OVX-induced bone loss, which is consistent with our *in vitro* findings. Mechanistically, previous research has revealed that TAK1 phosphorylates NF-κB-inducing kinase, resulting in the activation of the IκB kinase complex, which promotes osteoclastogenesis [35]. Phosphorylation of IκB-α enhances its ubiquitination and subsequent degradation [36]. Our findings further demonstrate that NaHS inhibits the phosphorylation of IκB-α, thereby inhibiting its ubiquitination and degradation. Generally, degradation of IκB-α promotes nuclear translocation of the NF-κB subunit p65 [37], a crucial step in enhancing osteoclast differentiation. By inhibiting nuclear p65 translocation, NaHS effectively disrupts this signaling pathway, ultimately suppressing osteoclastogenesis.

Our study, through *in vitro* and *in vivo* approaches, systematically elucidates for the first time the dual mechanisms by which the hydrogen sulfide donor NaHS inhibits osteoclast differentiation by regulating the NF-κB signaling pathway. Specifically, NaHS significantly suppresses IκB-α phosphorylation and prevents its ubiquitination-mediated degradation, thereby stabilizing the cytoplasmic anchoring of the NF-κB complex. In parallel, it blocks IKK-α/β activation and p65 nuclear translocation, ultimately leading to the downregulation of key osteoclastogenic transcription factors, such as c-Fos and NFATc1. These inhibitory effects were dose-dependent and further validated in the OVX osteoporosis model, where high-dose NaHS (1.5 mg/kg) restored mouse bone density to 60% of the baseline levels and reduced the number of osteoclasts by 46%. These observations provide a complementary mechanism for H_2S donors and reveal NaHS as a promising therapeutic candidate for osteoporosis.

NaHS serves as a donor of H_2S. Previous studies have revealed that garlic oil, identified as an H_2S donor, can suppress osteoporosis in ovariectomized rats and mice [38,39]. Compared with other H_2S donors, NaHS offers the advantage of rapid H_2S release and ease of experimental applications. However, its limitation lies in the instability of H_2S release, which can cause transient high concentrations and potential toxicity. To address this limitation, current research has focused on slow-release H_2S donors such as GYY4137, which slowly release H_2S and minimize the risk of local high concentration [40]. Other sulfur-containing compounds, like thiosulfate, also show antioxidant and anti-inflammatory effects, although their application is limited by low bioavailability and complex mechanisms of action [41].

Compared with traditional osteoporosis drugs, bisphosphonates (such as alendronate) directly inhibit osteoclast activity and are widely used in clinical practice. However, long-term use has been linked to bone fragility and side effects like gastrointestinal discomfort [42]. RANKL inhibitors (such as denosumab) show higher specificity by directly blocking osteoclast differentiation; however, their

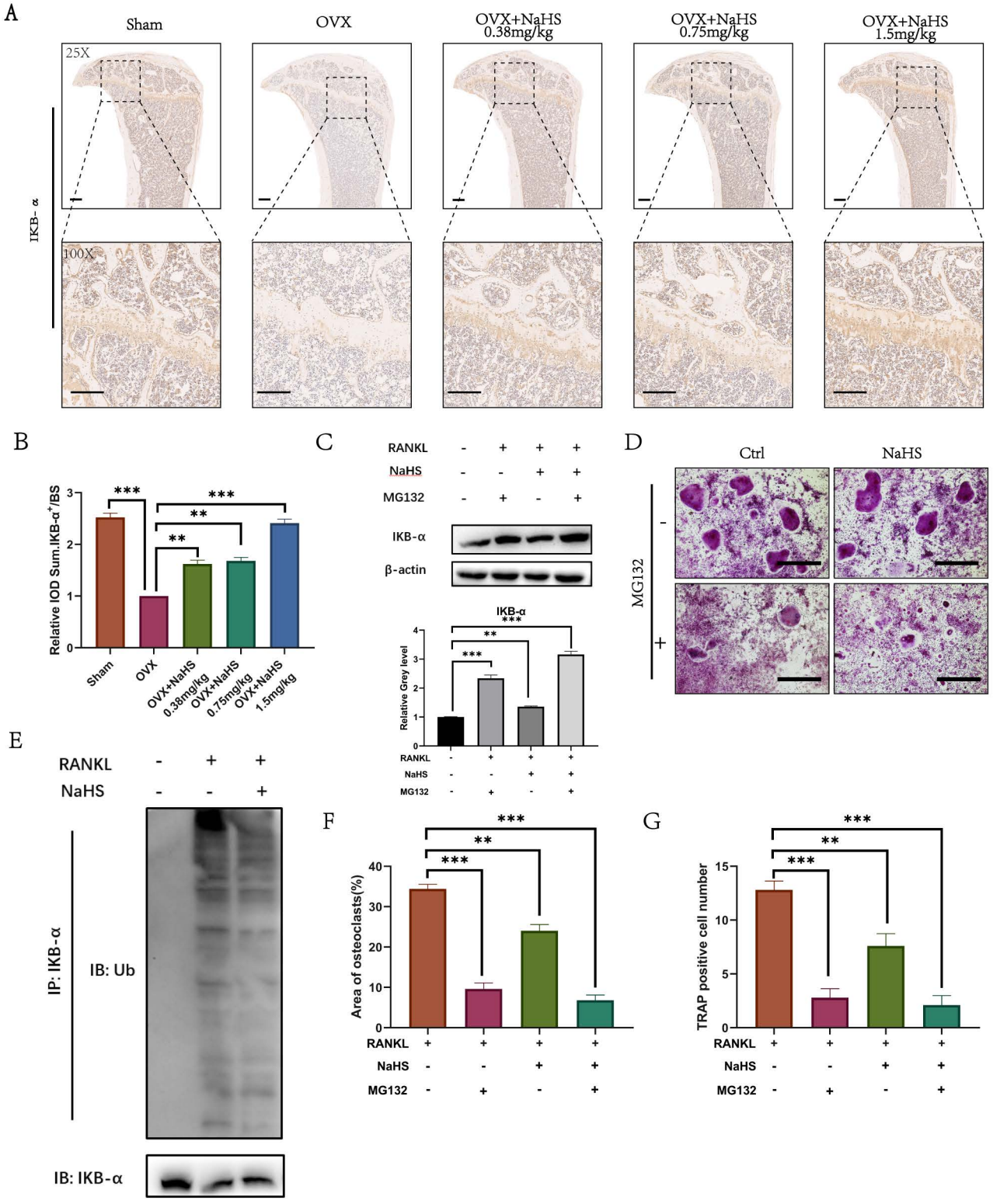

Fig. 6. NaHS inhibits ubiquitination and degradation of IκB-α. (A) IκB-α expression levels in the treated mice (n = 5). (B) Relative integrated optical density (IOD) sum of IκB-α+/BS was quantified in each group. (C) IκB-α expression in RAW264.7 cells incubated with the proteasomal inhibitor MG132 in the presence or absence of RANKL and NaHS. (D) TRAP-positive BMMs following the incubation with MG132 in the presence or absence of IκB-α. (E) RAW264.7 cells were incubated with RANKL and NaHS or untreated, and the ubiquitination level of IκB-α was assessed using western blot analysis. (F,G) Quantification of TRAP-positive cell number and area of osteoclasts. All experiments were performed at least three times. Scale bar = 100 µm. $^{**}p < 0.01$, $^{***}p < 0.005$. BS, bone surface; Ctrl, control; Ub, ubiquitination; IP, immunoprecipitation; IB, immunoblotting.

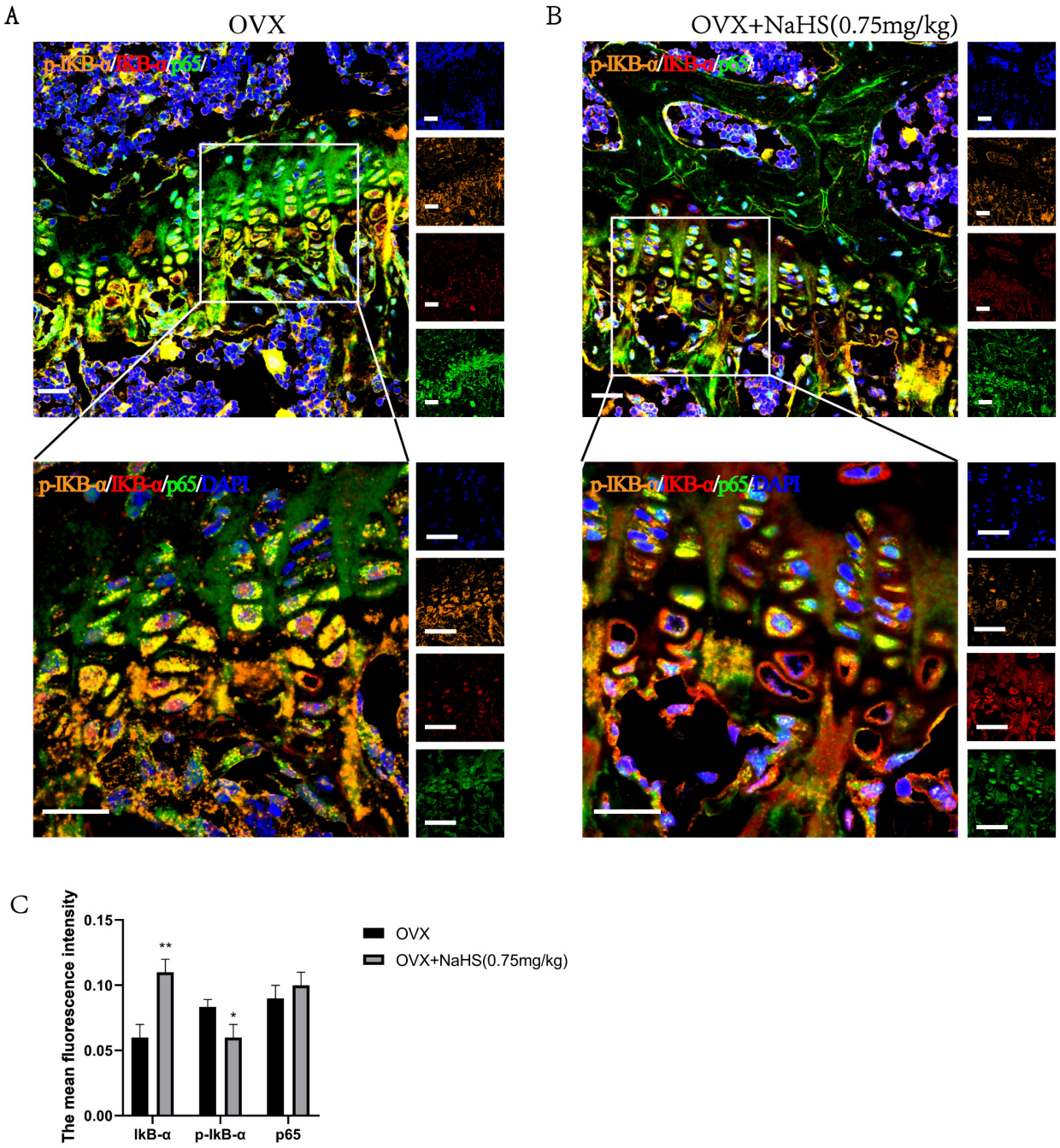

Fig. 7. NaHS inhibits degradation of IκB-α. (A) IκB-α, p-IκB-α, and p65 expression levels in the OVX mice (n = 5). (B) IκB-α. p-IκB-α, and p65 expression levels in the NaHS (0.75 mg/kg) treated mice (n = 5). (C) The mean fluorescence intensity of IκB-α, p-IκB-α, and p65. Scale bars = 100 μm. *$p < 0.05$, **$p < 0.01$.

high cost and risk of causing immunosuppression limit their widespread use. Conversely, NaHS not only inhibits osteoclast activity but has also been reported to exert anti-inflammatory and antioxidant effects [43,44]. However, its clinical application is impeded by the lack of validation studies and the inherent instability of H_2S release.

Although this study reveals the potential therapeutic value of NaHS, several limitations remain, primarily due to constraints in the experimental model and the concentration range applied. A reasonable concentration gradient of NaHS was applied to examine its specific effects on osteoclast formation; however, NaHS is known to decompose rapidly in culture medium [45]. Thus, its inhibitory effect on osteoclast formation is likely mediated through H_2S, a molecule generally regarded as toxic and still considered potentially harmful even at low concentrations despite its

crucial biological applications [46]. After NaHS treatment, the rapid release of H_2S may cause a transient increase in local concentration, leading to cell toxicity. High concentrations of H_2S can inhibit mitochondrial complex IV, disrupt cellular respiration, and induce oxidative stress and apoptosis. In many experimental settings, higher concentrations of NaHS (100–500 µM) are often used, which may exceed physiological levels and obscure its actual biological effects, thereby leading to variability in experimental outcomes. Therefore, to address these challenges, future studies should optimize NaHS dosage to approximate physiological concentrations (e.g., 10–50 µM) and investigate the use of slow-release H_2S donors (such as GYY4137), which can reduce peak instantaneous concentration increases and hence minimize toxicity.

In this study, we observed that NaHS inhibits osteoclast differentiation. However, whether this effect is mediated through H_2S-dependent inhibition of IκB-α ubiquitination and osteoclast activity remains to be fully explored. Most importantly, the impact of NaHS on osteoblast formation and its capability to improve bone formation in osteoporosis warrants further elucidation. NaHS has antioxidant and anti-inflammatory properties. Previous research has reported that H_2S enhances antioxidant capacity by activating the Nrf2 signaling pathway, thereby reducing oxidative stress-induced damage to osteoblasts [47]. Furthermore, NaHS inhibits the expression of inflammatory factors such as TNF-α and IL-6, improving the bone cell microenvironment [48]. Additionally, NaHS is also known to regulate calcium ion metabolism, as H_2S can promote osteoblast function by modulating intracellular calcium ion concentration (Ca^{2+}), affecting calcium transport proteins, including Ca^{2+}-ATPase, which promote bone mineralization. Although the precise mechanisms of NaHS in bone remodeling remain poorly understood, evidence from this and previous studies indicates that inhibition of NF-κB-dependent transcription in conjunction with suppression of IκB-α ubiquitination and degradation contributes to the blockade of RANKL-induced osteoclast formation [49,50].

However, we must also consider the off-target effects of NaHS, as it acts as a H_2S donor, and its broad biological activity increases concerns regarding possible off-target effects across different concentrations and tissues. H_2S demonstrates concentration-dependent dual roles in the cardiovascular system [51]. At low concentrations, it promotes vasodilation and exerts anti-inflammatory and antioxidant effects at high concentrations, it can damage vascular endothelial cells and trigger oxidative stress [52,53]. The rapid release of H_2S from NaHS may lead to excessively high local concentrations, inducing endothelial cell dysfunction. Similarly, H_2S has been found to have neuroprotective effects in the central nervous system, regulating synaptic transmission and anti-inflammatory responses.

In contrast, high concentrations of NaHS may cause neurotoxicity, manifesting through oxidative stress and mitochondrial dysfunction [54,55]. Furthermore, NaHS can affect redox balance in hepatocytes and renal cells. High concentrations of H_2S may inhibit mitochondrial respiratory chains in hepatocytes, leading to cell damage. Additionally, the kidneys are particularly sensitive to H_2S, where excess exposure may cause tubular injury and inflammatory responses [56]. Additionally, NaHS also influences immune responses by modulating macrophage polarization (M1/M2). High H_2S concentrations can aberrantly activate inflammatory signaling pathways, resulting in excessive immune cell responses [57].

Moreover, the inherent instability of NaHS significantly affects both its bioavailability and the reproducibility of results. NaHS rapidly decomposes in aqueous solutions, making it difficult to accurately control H_2S release. *In vivo*, the complex metabolic environment further alleviates its bioavailability, contributing to variability in outcomes and complicating precise assessment of its effects. Therefore, future studies may benefit from the use of sustained-release H_2S donors (such as GYY4137) to improve stability, along with real-time monitoring of H_2S concentration using fluorescent probe technology to assess the release dynamics. Furthermore, using computational simulations to predict NaHS metabolism and distribution *in vivo* could further enhance experimental consistency and facilitate a more precise evaluation of its therapeutic potential.

Conclusions

This study demonstrates that NaHS regulates bone metabolism by inhibiting NF-κB nuclear translocation and suppressing osteoclast differentiation, an effect likely mediated through the inhibition of IκB-α phosphorylation and ubiquitination-dependent degradation. Furthermore, this study identifies NaHS as a potential candidate for the treatment of osteoporosis. Beyond expanding the pharmacological framework of H_2S donors, it also reveals a novel molecular connection between sulfur metabolism and bone homeostasis. Future research should validate target specificity using osteoclast-specific IκB-α mutant mice and explore potential synergistic effects of NaHS in combination with existing anti-osteoporosis drugs, thereby laying the foundation for developing combination treatment regimens based on sulfur signal regulation.

Abbreviations

CCK-8, cell counting kit-8; BMMs, bone marrow-derived macrophages; TRAP, tartrate-resistant acid phosphatase; RANKL, receptor activator of nuclear factor-κB ligand; OVX, ovariectomy; BMD, bone mineral density; BV/TV, bone volume to total volume ratio; BS/BV, bone surface-to-volume ratio; Tb.Sp, trabecular separation; Tb.N, trabecular number; Tb.Th, trabecular thickness; KEGG, Kyoto Encyclopedia of Genes and Genomes; GO, Gene Ontology.

Availability of Data and Materials

The datasets used and analyzed during the current study are available from the corresponding authors on reasonable request.

Author Contributions

YHL and YH designed the research and interpreted the data. WCF, WQT and KX performed the experiments. WQT and KX analyzed the data. WCF wrote the original manuscript. WQT reviewed and edited the manuscript. WQT and YHL finalized the manuscript. All authors contributed to important editorial changes in the manuscript and approved the final manuscript. All authors have participated sufficiently in the work and agreed to be accountable for all aspects of the work.

Ethics Approval and Consent to Participate

The approval of this study was authorized by the Fifth People's Hospital of Shanghai, Fudan University, China. Animals were sacrificed according to specified standards. Animal ethics number: 2020-WY-JS063.

Acknowledgment

We thank the Experimental Center of the Fifth People's Hospital of Shanghai for providing experimental instruments and reagents.

Funding

This work was supported by the Shanghai Science and Technology Innovation Action Plan Natural-Science Foundation Project (Grant No.23ZR1449800); Excellent Academic Leader Program of Shanghai Science and Technology Commission (Grant No.20XD1402700); Minhang Natural Science Foundation Project (Grant No.2019MHZ071) and Research program of the Fifth People's Hospital of Shanghai, Fudan University (Grant No. 2019WYZD01).

Conflict of Interest

The authors declare no conflict of interest.

Supplementary Material

Supplementary material associated with this article can be found, in the online version, at https://doi.org/10.24976/Discov.Med.202537201.207.

References

[1] Compston JE, McClung MR, Leslie WD. Osteoporosis. Lancet (London, England). 2019; 393: 364–376. https://doi.org/10.1016/S0140-6736(18)32112-3.

[2] Ensrud KE, Crandall CJ. Osteoporosis. Annals of Internal Medicine. 2017; 167: ITC17–ITC32. https://doi.org/10.7326/AITC201708010.

[3] Schacter GI, Leslie WD. Diabetes and Osteoporosis: Part II, Clinical Management. Endocrinology and Metabolism Clinics of North America. 2021; 50: 287–297. https://doi.org/10.1016/j.ecl.2021.03.006.

[4] Marjoribanks J, Farquhar C, Roberts H, Lethaby A, Lee J. Long-term hormone therapy for perimenopausal and postmenopausal women. The Cochrane Database of Systematic Reviews. 2017; 1: CD004143. https://doi.org/10.1002/14651858.CD004143.pub5.

[5] Harris K, Zagar CA, Lawrence KV. Osteoporosis: Common Questions and Answers. American Family Physician. 2023; 107: 238–246.

[6] Anam AK, Insogna K. Update on Osteoporosis Screening and Management. The Medical Clinics of North America. 2021; 105: 1117–1134. https://doi.org/10.1016/j.mcna.2021.05.016.

[7] Sinder BP, Pettit AR, McCauley LK. Macrophages: Their Emerging Roles in Bone. Journal of Bone and Mineral Research: the Official Journal of the American Society for Bone and Mineral Research. 2015; 30: 2140–2149. https://doi.org/10.1002/jbmr.2735.

[8] Huang W, Gong Y, Yan L. ER Stress, the Unfolded Protein Response and Osteoclastogenesis: A Review. Biomolecules. 2023; 13: 1050. https://doi.org/10.3390/biom13071050.

[9] Ono T, Hayashi M, Sasaki F, Nakashima T. RANKL biology: bone metabolism, the immune system, and beyond. Inflammation and Regeneration. 2020; 40: 2. https://doi.org/10.1186/s41232-019-0111-3.

[10] Bai S, Kitaura H, Zhao H, Chen J, Müller JM, Schüle R, *et al*. FHL2 inhibits the activated osteoclast in a TRAF6-dependent manner. The Journal of Clinical Investigation. 2005; 115: 2742–2751. https://doi.org/10.1172/JCI24921.

[11] Karin M, Ben-Neriah Y. Phosphorylation meets ubiquitination: the control of NF-[kappa]B activity. Annual Review of Immunology. 2000; 18: 621–663. https://doi.org/10.1146/annurev.immunol.18.1.621.

[12] Clézardin P, Coleman R, Puppo M, Ottewell P, Bonnelye E, Paycha F, *et al*. Bone metastasis: mechanisms, therapies, and biomarkers. Physiological Reviews. 2021; 101: 797–855. https://doi.org/10.1152/physrev.00012.2019.

[13] Takayanagi H. The role of NFAT in osteoclast formation. Annals of the New York Academy of Sciences. 2007; 1116: 227–237. https://doi.org/10.1196/annals.1402.071.

[14] Zheng H, Liu Y, Deng Y, Li Y, Liu S, Yang Y, *et al*. Recent advances of NFATc1 in rheumatoid arthritis-related bone destruction: mechanisms and potential therapeutic targets. Molecular Medicine (Cambridge, Mass.). 2024; 30: 20. https://doi.org/10.1186/s10020-024-00788-w.

[15] Jiang T, Xia T, Qiao F, Wang N, Jiang Y, Xin H. Role and Regulation of Transcription Factors in Osteoclastogenesis. International Journal of Molecular Sciences. 2023; 24: 16175. https://doi.org/10.3390/ijms242216175.

[16] Yang W, Lu X, Zhang T, Han W, Li J, He W, *et al*. TAZ inhibits osteoclastogenesis by attenuating TAK1/NF-κB signaling. Bone Research. 2021; 9: 33. https://doi.org/10.1038/s41413-021-00151-3.

[17] Xiao Y, Xie X, Chen Z, Yin G, Kong W, Zhou J. Advances in the roles of ATF4 in osteoporosis. Biomedicine & Pharmacotherapy = Biomedecine & Pharmacotherapie. 2023; 169: 115864. https://doi.org/10.1016/j.biopha.2023.115864.

[18] Bertolucci V, Ninomiya AF, Longato GB, Kaneko LO, Nonose N, Scariot PPM, *et al*. Bioactive Compounds from Propolis on Bone Homeostasis: A Narrative Review. Antioxidants (Basel, Switzerland). 2025; 14: 81. https://doi.org/10.3390/antiox14010081.

[19] Kashiba M, Kajimura M, Goda N, Suematsu M. From O2 to H2S: a landscape view of gas biology. The Keio Journal of Medicine. 2002; 51: 1–10. https://doi.org/10.2302/kjm.51.1.

[20] Kajimura M, Fukuda R, Bateman RM, Yamamoto T, Suematsu M. Interactions of multiple gas-transducing systems: hallmarks and uncertainties of CO, NO, and H2S gas biology. Antioxidants & Redox Signaling. 2010; 13: 157–192. https://doi.org/10.1089/ars.2009.2657.

[21] Vandiver MS, Snyder SH. Hydrogen sulfide: a gasotransmitter of clinical relevance. Journal of Molecular Medicine (Berlin, Germany). 2012; 90: 255–263. https://doi.org/10.1007/s00109-012-0873-4.

[22] Jiang M, Wang T, Yan X, Liu Z, Yan Y, Yang K, *et al*. A Novel Rhein Derivative Modulates Bone Formation and Resorption and Ameliorates Estrogen-Dependent Bone Loss. Journal of Bone and Mineral Research: the Official Journal of the American Society for Bone and Mineral Research. 2019; 34: 361–374. https://doi.org/10.1002/jbmr.3604.

[23] Kurabayashi M. Hydrogen sulfide: a new regulator of osteoclastogenesis? Arteriosclerosis, Thrombosis, and Vascular Biology. 2014; 34: 471–473. https://doi.org/10.1161/ATVBAHA.114.303072.

[24] Irie K, Ekuni D, Yamamoto T, Morita M, Yaegaki K, Ii H, *et al*. A single application of hydrogen sulphide induces a transient osteoclast differentiation with RANKL expression in the rat model. Archives of Oral Biology. 2009; 54: 723–729. https://doi.org/10.1016/j.archoralbio.2009.05.006.

[25] Yang J, Tang R, Yi J, Chen Y, Li X, Yu T, *et al*. Diallyl disulfide alleviates inflammatory osteolysis by suppressing osteoclastogenesis *via* NF-κB-NFATc1 signal pathway. FASEB Journal: Official Publication of the Federation of American Societies for Experimental Biology. 2019; 33: 7261–7273. https://doi.org/10.1096/fj.201802172R.

[26] Jiang L, Wu Y, Xu Z, Hou M, Chen S, Cheng C, *et al*. Harnessing hydrogen sulfide in injectable hydrogels that guide the immune response and osteoclastogenesis balance for osteoporosis treatment. Materials Today Bio. 2024; 29: 101338. https://doi.org/10.1016/j.mtbio.2024.101338.

[27] Dong Y, Kang H, Peng R, Liu Z, Liao F, Hu SA, *et al*. A clinical-stage Nrf2 activator suppresses osteoclast differentiation via the iron-ornithine axis. Cell Metabolism. 2024; 36: 1679–1695.e6. https://doi.org/10.1016/j.cmet.2024.03.005.

[28] Komori T. Animal models for osteoporosis. European Journal of Pharmacology. 2015; 759: 287–294. https://doi.org/10.1016/j.ejphar.2015.03.028.

[29] Liu F, Yuan L, Li L, Yang J, Liu J, Chen Y, *et al*. S-sulfhydration of SIRT3 combats BMSC senescence and ameliorates osteoporosis via stabilizing heterochromatic and mitochondrial homeostasis. Pharmacological Research. 2023; 192: 106788. https://doi.org/10.1016/j.phrs.2023.106788.

[30] Jia Z, Zhang X, Li Z, Yan H, Tian X, Luo C, *et al*. Hydrogen sulfide mitigates ox LDL induced NLRP3/caspase 1/GSDMD dependent macrophage pyroptosis by S sulfhydrating caspase 1. Molecular Medicine Reports. 2024; 30: 135. https://doi.org/10.3892/mmr.2024.13259.

[31] Shishodia S, Gutierrez AM, Lotan R, Aggarwal BB. N-(4-hydroxyphenyl) retinamide inhibits invasion, suppresses osteoclastogenesis, and potentiates apoptosis through down-regulation of I(kappa)B(alpha) kinase and nuclear factor-kappaB-regulated gene products. Cancer Research. 2005; 65: 9555–9565. https://doi.org/10.1158/0008-5472.CAN-05-1585.

[32] Black DM, Greenspan SL, Ensrud KE, Palermo L, McGowan JA, Lang TF, *et al*. The effects of parathyroid hormone and alendronate alone or in combination in postmenopausal osteoporosis. The New England Journal of Medicine. 2003; 349: 1207–1215. https://doi.org/10.1056/NEJMoa031975.

[33] Lobo RA. Hormone-replacement therapy: current thinking. Nature Reviews. Endocrinology. 2017; 13: 220–231. https://doi.org/10.1038/nrendo.2016.164.

[34] Li H, Xiao Z, Quarles LD, Li W. Osteoporosis: Mechanism, Molecular Target and Current Status on Drug Development. Current Medicinal Chemistry. 2021; 28: 1489–1507. https://doi.org/10.2174/0929867327666200330142432.

[35] Ajibade AA, Wang HY, Wang RF. Cell type-specific function of TAK1 in innate immune signaling. Trends in Immunology. 2013; 34: 307–316. https://doi.org/10.1016/j.it.2013.03.007.

[36] Skaug B, Jiang X, Chen ZJ. The role of ubiquitin in NF-kappaB regulatory pathways. Annual Review of Biochemistry. 2009; 78: 769–796. https://doi.org/10.1146/annurev.biochem.78.070907.102750.

[37] Yee YH, Chong SJF, Kong LR, Goh BC, Pervaiz S. Sustained IKKβ phosphorylation and NF-κB activation by superoxide-induced peroxynitrite-mediated nitrotyrosine modification of B56γ3 and PP2A inactivation. Redox Biology. 2021; 41: 101834. https://doi.org/10.1016/j.redox.2020.101834.

[38] Predmore BL, Kondo K, Bhushan S, Zlatopolsky MA, King AL, Aragon JP, *et al*. The polysulfide diallyl trisulfide protects the ischemic myocardium by preservation of endogenous hydrogen sulfide and increasing nitric oxide bioavailability. American Journal of Physiology. Heart and Circulatory Physiology. 2012; 302: H2410–8. https://doi.org/10.1152/ajpheart.00044.2012.

[39] Mukherjee M, Das AS, Mitra S, Mitra C. Prevention of bone loss by oil extract of garlic (Allium sativum Linn.) in an ovariectomized rat model of osteoporosis. Phytotherapy Research: PTR. 2004; 18: 389–394. https://doi.org/10.1002/ptr.1448.

[40] Ma J, Yang P, Zhou Z, Song T, Jia L, Ye X, *et al*. GYY4137-induced p65 sulfhydration protects synovial macrophages against pyroptosis by improving mitochondrial function in osteoarthritis development. Journal of Advanced Research. 2025; 71: 173–188. https://doi.org/10.1016/j.jare.2024.05.033.

[41] Tang SM, Lu GZ, Lei XY, Yang XY, Tang GT, Yu J, *et al*. Sodium thiosulfate: A donor or carrier signaling molecule for hydrogen sulfide? Nitric Oxide: Biology and Chemistry. 2024; 149: 67–74. https://doi.org/10.1016/j.niox.2024.06.004.

[42] de Villiers TJ. Bone health and menopause: Osteoporosis prevention and treatment. Best Practice & Research. Clinical Endocrinology & Metabolism. 2024; 38: 101782. https://doi.org/10.1016/j.beem.2023.101782.

[43] Yu L, Luo Q, Rao X, Xiao X, Wang P. Unveiling the anti-inflammatory mechanism of exogenous hydrogen sulfide in Kawasaki disease based on network pharmacology and experimental validation. Scientific Reports. 2025; 15: 7410. https://doi.org/10.1038/s41598-025-91998-7.

[44] Benedetti F, Curreli S, Krishnan S, Davinelli S, Cocchi F, Scapagnini G, *et al*. Anti-inflammatory effects of H_2S during acute bacterial infection: a review. Journal of Translational Medicine. 2017; 15: 100. https://doi.org/10.1186/s12967-017-1206-8.

[45] Trummer M, Galardon E, Fischer A, Toegel S, Mayer B, Steiner G, *et al*. Characterization of the Inducible and Slow-Releasing Hydrogen Sulfide and Persulfide Donor P*: Insights into Hydrogen Sulfide Signaling. Antioxidants (Basel, Switzerland). 2021; 10: 1049. https://doi.org/10.3390/antiox10071049.

[46] Bouillaud F, Blachier F. Mitochondria and sulfide: a very old story of poisoning, feeding, and signaling? Antioxidants & Redox Signaling. 2011; 15: 379–391. https://doi.org/10.1089/ars.2010.3678.

[47] Hamidizad Z, Kadkhodaee M, Karimian SM, Ranjbaran M, Heidari F, Bakhshi E, *et al*. Therapeutic effects of CORM3 and NaHS in chronic kidney disease induced cognitive impairment via the interaction between carbon monoxide and hydrogen sulfide on Nrf2/HO-1 signaling pathway in rats. Chemico-

Biological Interactions. 2022; 368: 110217. https://doi.org/10.1016/j.cbi.2022.110217.

[48] Yin J, Tu C, Zhao J, Ou D, Chen G, Liu Y, *et al*. Exogenous hydrogen sulfide protects against global cerebral ischemia/reperfusion injury via its anti-oxidative, anti-inflammatory and anti-apoptotic effects in rats. Brain Research. 2013; 1491: 188–196. https://doi.org/10.1016/j.brainres.2012.10.046.

[49] Baud V, Karin M. Is NF-kappaB a good target for cancer therapy? Hopes and pitfalls. Nature Reviews. Drug Discovery. 2009; 8: 33–40. https://doi.org/10.1038/nrd2781.

[50] Jimi E, Aoki K, Saito H, D'Acquisto F, May MJ, Nakamura I, *et al*. Selective inhibition of NF-kappa B blocks osteoclastogenesis and prevents inflammatory bone destruction in vivo. Nature Medicine. 2004; 10: 617–624. https://doi.org/10.1038/nm1054.

[51] Sun Y, Tang CS, DU JB, Jin HF. Hydrogen sulfide and vascular relaxation. Chinese Medical Journal. 2011; 124: 3816–3819.

[52] Zhang L, Wang Y, Li Y, Li L, Xu S, Feng X, *et al*. Hydrogen Sulfide (H_2S)-Releasing Compounds: Therapeutic Potential in Cardiovascular Diseases. Frontiers in Pharmacology. 2018; 9: 1066. https://doi.org/10.3389/fphar.2018.01066.

[53] Tian D, Teng X, Jin S, Chen Y, Xue H, Xiao L, *et al*. Endogenous hydrogen sulfide improves vascular remodeling through PPARδ/SOCS3 signaling. Journal of Advanced Research. 2020; 27: 115–125. https://doi.org/10.1016/j.jare.2020.06.005.

[54] Wang JF, Li Y, Song JN, Pang HG. Role of hydrogen sulfide in secondary neuronal injury. Neurochemistry International. 2014; 64: 37–47. https://doi.org/10.1016/j.neuint.2013.11.002.

[55] Wei HJ, Tan HY, Cao JP, He J, Zhang QL, Jiang L, *et al*. Therapeutic importance of hydrogen sulfide in cognitive impairment diseases. Brain Research. 2025; 1856: 149547. https://doi.org/10.1016/j.brainres.2025.149547.

[56] McCook O, Radermacher P, Volani C, Asfar P, Ignatius A, Kemmler J, *et al*. H2S during circulatory shock: some unresolved questions. Nitric Oxide: Biology and Chemistry. 2014; 41: 48–61. https://doi.org/10.1016/j.niox.2014.03.163.

[57] Zhang H, Bhatia M. Hydrogen sulfide: a novel mediator of leukocyte activation. Immunopharmacology and Immunotoxicology. 2008; 30: 631–645. https://doi.org/10.1080/08923970802278045.